Assessment of a Variational Inversion System for Rainfall Rate Over Land and Water Surfaces

Flavio Iturbide-Sanchez, *Member, IEEE*, Sid-Ahmed Boukabara, Ruiyue Chen, Kevin Garrett, Christopher Grassotti, Wanchun Chen, and Fuzhong Weng

***Abstract*—A comprehensive system that is used to invert the geophysical products from microwave measurements has recently been developed. This system, known as the Microwave Integrated Retrieval System (MiRS), ensures that the final solution is consistent with the measurements and, when used as input to the forward operator, fits them to within the instrument noise levels. In the presence of precipitation, this variational algorithm retrieves a set of hydrometeor products consisting of cloud liquid water, ice water, and rain water content profiles. This paper presents the development and assessment of the MiRS rainfall rate that is derived based on a predetermined relationship of the rainfall with these hydrometeor products. Since this relationship relies on the geophysical products retrieved by the MiRS as inputs and not on sensor-dependent parameters, the technique is suitable for all microwave sensors to which the MiRS is applied. This precipitation technique has been designed to facilitate its transition from research to operations when applied to current and future satellite-based sensors. Currently, the MiRS rainfall rate technique has been implemented operationally at the U.S. National Oceanic and Atmospheric Administration (NOAA) for the NOAA-18, NOAA-19, Metop-A Advanced Microwave Sounding Unit, and Microwave Humidity Sensor, as well as for the Defense Meteorological Satellite Program (DMSP)-F16 and DMSP-F18 Special Sensor Microwave Imager/Sounder microwave satellite sensors. For the validation of the MiRS rainfall rate technique, extensive comparisons with state-of-the-art precipitation products derived from rain gauge, ground-based radar, and satellite-based microwave observations are presented for different regions and seasons, and over land and ocean. The MiRS rainfall rate technique is shown to estimate precipitation, with a skill comparable to other satellite-based microwave precipitation algorithms, including the MSPPS, 3B40RT, and MWCOMB, while showing no discontinuities at coasts. This is a relevant result, considering that the MiRS is a system not merely designed to retrieve the rainfall rate but to consistently estimate a comprehensive set of atmospheric and surface parameters from microwave measurements.**

Manuscript received June 30, 2010; revised November 8, 2010 and January 11, 2011; accepted January 16, 2011. Date of publication May 23, 2011; date of current version August 26, 2011. This work was supported by the U.S. National Oceanic and Atmospheric Administration (NOAA) Office of Systems Development (OSD) Product Systems Development Implementation (PSDI). The views expressed here are solely those of the authors and do not constitute a statement of policy, decision, or position on behalf of NOAA or the U.S. Government.

F. Iturbide-Sanchez, R. Chen, K. Garrett, and C. Grassotti are with the I. M. Systems Group, Inc., at the NOAA/NESDIS/Center for Satellite Applications and Research, Camp Springs, MD 20746 USA (e-mail: Flavio.Iturbide@noaa.gov; Ruiyue.Chen@noaa.gov; kevin.garrett@noaa.gov; Christopher.Grassotti@noaa.gov).

S.-A. Boukabara and F. Weng are with the National Oceanic and Atmospheric Administration Center for Satellite Applications and Research, Camp Springs, MD 20746 USA (e-mail: sid.boukabara@noaa.gov; fuzhong.weng@noaa.gov).

W. Chen is with Dell Inc., Camp Springs, MD 20746 USA (e-mail: wanchun.chen@noaa.gov).

Color versions of one or more of the figures in this paper are available online at http://ieeexplore.ieee.org.

Digital Object Identifier 10.1109/TGRS.2011.2119375

***Index Terms*—Microwave radiometry, rain, remote sensing, satellites.**

I. Introduction

MEASUREMENTS of precipitation on different time and space scales are essential for a variety of research areas that provide an inherent benefit to human society as well as contribute to improved understanding of the global ecological system. The release of latent heat by precipitation represents the major source of energy for atmospheric circulation systems and plays a key role in the formation of destructive storms such as tropical cyclones and severe thunderstorms. In this respect, precipitation observations provide significant information about the water cycle and the distribution of the Earth's latent heating that can be used to improve the forecast of severe events and to provide valuable information for disaster mitigation.

Due to the large variability of the precipitation in time and space, precipitation is one of the most difficult atmospheric parameters to measure. Currently, accurate precipitation measurements rely on rain gauges and ground-based radar observations. One of the major disadvantages of these precipitation measurements is related to their intrinsic spatial and temporal sampling characteristics. For example, unless they are deployed in a dense network, rain gauges are point measurements that cannot provide rain measurements representative over larger regions. Moreover, rain gauges and ground-based radars can only cover a small portion of the global land areas and are generally unable to be deployed over ocean surfaces. In recent years, satellite-based sensors and systems have also shown their capability to obtain reliable precipitation measurements on a global scale, including both land and ocean surfaces. These measurements have contributed to improvements in precipitation observations, which, in turn, have led to an enhancement in the knowledge and understanding of hydrological processes and global energy budget.

In this paper, we present a new method for precipitation estimation over land and ocean surfaces based on a variational inversion system that, first, directly retrieves a relatively complete geophysical state, including the hydrometeor profiles, and, subsequently, the associated surface rainfall rate.

II. Satellite-Based Precipitation Estimates

A. Overview of the Satellite-Based Retrieval Algorithms

The development of precipitation estimation techniques from satellite-based observations was initiated with the advent of

meteorological satellites during the 1970s. Since then, the use of meteorological satellites to estimate precipitation has increased significantly, particularly in the last decades, mainly due to the increased number of specialized precipitation satellite missions, such as the Tropical Rainfall Measuring Mission (TRMM) that is designed to monitor and study tropical rainfall [1], and the development and improvement of the communication infrastructure, which has allowed meteorological centers to more easily receive and process data from multiple satellite platforms.

The first satellite-based precipitation estimation techniques used visible or infrared (IR) observations to estimate precipitation intensity from the visible reflectivity of the clouds and cloud top temperature, as is the case of one of the early techniques reported in [2]. One of the major advantages of the satellite-based IR precipitation techniques is associated with its relatively high temporal and spatial resolution. However, visible or IR-based precipitation techniques tend to have large uncertainties, particularly for short-term or instantaneous estimates of precipitation, due to the weak relationship found between the cloud properties observed (e.g., cloud top temperature and reflectivity) and precipitation. On the other hand, due to the successful deployment of passive microwave sensors on polar-orbiting satellites, precipitation estimates based on microwave observations became available soon after the development of the IR precipitation techniques, representing a significant advancement in the measurement of the precipitation fields. Microwave-based methods provide more accurate precipitation estimates due to the strong physical relationship that exists between atmospheric microwave observations and precipitation. A comprehensive study of the various algorithms for the retrieval of rainfall from passive microwave measurements from the Special Sensor Microwave Imager (SSM/I) is presented in [3]. In [4], a regression-based algorithm based on the ice water path (IWP) and a rain type classification is used to estimate the precipitation over ocean and land surfaces. Examples of the physical inversion-based precipitation algorithms can be found in [5] and [6]. Recently, the development of a global precipitation retrieval algorithm for the Advanced Microwave Sounding Unit (AMSU) is presented in [7]. The performance of this paper relies on physical models, including the Goddard cloud resolving physics model and the fifth-generation Pennsylvania State University and the National Center for Atmospheric Research Mesoscale Model (MM5).

The first results describing a successful method that combines satellite-based passive microwave and IR observations to estimate precipitation are reported in [8]. The strength of the method based on the synergy of the microwave and IR observations to estimate precipitation relies on the efficient use of the high spatial and temporal resolution (important in capturing the patterns of the highly variable precipitation) associated with the IR observations and the strong relationship found between the measured radiances and precipitation obtained from the microwave observations. Some examples of works related to the development of techniques based on both the IR and microwave observations to estimate precipitation include the Climate Prediction Center morphing method [9], the Moderate Resolution Imaging Spectroradiometer (MODIS) and Advanced Microwave Scanning Radiometer for Earth Observing System (AMSR-E) blended data technique [10], the TRMM Multisatellite Precipitation Analysis [11], and the Global Satellite Mapping of Precipitation Kalman filter-based (GSMaP_MVK) method [12]. As a consequence of these developments, several satellite-based rainfall products are now available in near real time, providing the distributions of the rainfall rate on a global scale.

Significant efforts to evaluate the performance of satellite precipitation retrieval algorithms have led to the implementation of intercomparison programs such as the Global Precipitation Climatology Project [13], [14], the WetNet Precipitation Intercomparison Project [15]–[17], the International Precipitation Working Group (IPWG) [18], and the Program for the Evaluation of High-Resolution Precipitation Products [19] that was conceived as a broader formalization of the existing IPWG validation effort. These studies have contributed to the improvement of existing precipitation retrieval algorithms, making them more robust and sophisticated.

B. Satellite-Based Passive Microwave Retrieval Algorithms

Most current precipitation algorithms based on passive microwave observations derive surface rain rates from measured brightness temperatures using different schemes, including statistical deterministic, quasi-physical deterministic, physical deterministic, and physical inversion profile techniques. Of these techniques, the first two require an empirical calibration with respect to a precipitation reference, such as rain gauges or weather radars. Additionally, the first technique is based on regression schemes, while the other techniques are based on radiative transfer (RT) modeling. For the particular case of the physical inversion profile technique, an adjustment of the value of the surface precipitation is generally performed until the calculated brightness temperatures from a forward RT model are consistent with the measured brightness temperatures. The precipitation estimation technique presented in this paper relies mainly on a physical-based retrieval system to first retrieve cloud liquid water (CLW) and rain and ice water that, later on, are used as predictors to estimate the rainfall rate using a linear regression scheme.

The capability of current satellite-based precipitation algorithms to retrieve precipitation from measured brightness temperatures depends highly on the appropriate selection of the channels to be used. For example, channels at frequencies near or below 37 GHz, often referred to as emission channels, measure precipitation mainly due to the energy emitted by raindrops. The brightness temperatures at this frequency are somewhat less affected by scattering related to ice particles when compared to higher frequencies. On the other hand, the brightness temperatures observed near 85 GHz, which are also sensitive to pure emission processes, are also more highly affected by scattering of radiation due to ice particles (if they exist) above the freezing level.

The development of new satellite-based microwave sensors, planned as part of future missions, will utilize new and more channels [20]–[22]. New rainfall rate algorithms need to be implemented in order to take advantage of the

enhanced design of new microwave sensors. In this regard, the implementation of a precipitation algorithm that does not highly depend on a set of specific channels has certain advantages, particularly when the algorithm is intended to be applied to multiple satellite platforms and sensors that have been designed using different architectures. The necessity of a generic precipitation estimation algorithm that can facilitate its transition from research to operations and can potentially be applied on current and future sensors has motivated the development of the precipitation algorithm presented in this paper.

III. MiRS

A. Overview of the MiRS

The Microwave Integrated Retrieval System (MiRS) is a physically based retrieval system that uses a 1-D variational (1-DVAR) retrieval scheme to solve simultaneously for surface and atmospheric parameters, including hydrometeors [23], [24]. The MiRS system is an iterative physical inversion system that inverts the RT equation by simultaneously finding radiometrically appropriate profiles of temperature, water vapor, liquid cloud, and hydrometeors, as well as the surface emissivity spectrum and skin temperature. The addition of the emissivity spectrum in the state vector makes the system applicable globally, with the only differences between land, ocean, sea-ice, and snow backgrounds residing in the mean values and covariance matrix chosen to spectrally constrain the emissivity. Moreover, the inclusion of the cloud and hydrometeor parameters within the state vector makes the inversion of the cloudy and rainy radiances possible, therefore providing an all-weather capability to the system. By performing simple vertical integration, the retrieved hydrometeor profiles are used to compute the CLW path (CLWP), IWP, and rain water path (RWP). In an additional postprocessing step, other products are derived, e.g., the surface rainfall rate based on the hydrometeor parameters (the focus of this paper) or the surface snow and ice properties that are based on the retrieved surface emissivity vector.

The MiRS system was implemented operationally for the first time at the U.S. National Oceanic and Atmospheric Administration (NOAA) in 2007 for the NOAA-18 satellite. Since then, the MiRS has been applied operationally for NOAA-19, Metop-A AMSU and Microwave Humidity Sensor (MHS), Defense Meteorological Satellite Program (DMSP) F16 SSM/I/Sounder (SSMIS), and, most recently, DMSP-F18 SSMI/S.

B. 1-DVAR Approach

In general, given *a priori* or background information on the atmosphere and surface, a set of observed brightness temperatures, and a forward operator that is capable of simulating brightness temperatures based on the specification of the atmospheric state, a 1-DVAR retrieval algorithm is able to combine this information to determine the best estimate of the state of the atmosphere [25]. The iterative process of the 1-DVAR inversion scheme employed by the MiRS aims at minimizing the cost function $J(X)$, which is given as

$$J(X) = \left[\frac{1}{2}(X - X_0)^T \times B^{-1} \times (X - X_0)\right] + \left[\frac{1}{2}\left(Y^m - Y(X)\right)^T \times E^{-1} \times \left(Y^m - Y(X)\right)\right] \quad (1)$$

where X in the first term on the right of (1) is the retrieved state vector, and the term itself represents the penalty for departing from the background X_0, weighted by the error covariance matrix B. The second term in (1) represents the penalty for the simulated radiances Y departing from the observed radiances Y^m, weighted by instrument and modeling errors E. The minimization of $J(X)$ is also the basis for variational analysis retrieval. The solution that minimizes this two-term cost function is sometimes referred to as a constrained solution and is given as follows:

$$\Delta X_{n+1} = \left\{BK_n^T\left(K_nBK_n^T + E\right)^{-1}\right\} \times \left[\left(Y^m - Y(X_n)\right) + K_n\Delta X_n\right] \quad (2)$$

where ΔX is the updated state vector at iteration $n+1$ and K is the matrix of Jacobians which contain the sensitivity of X (parameters to retrieve) to the radiances. The geophysical vector X is retrieved as one entity, including the temperature, moisture, and atmospheric hydrometeor profiles, as well as skin surface temperature and surface emissivity vector, ensuring a consistent solution that fits the radiances. The covariance matrix B is composed of atmospheric, hydrometeor, and surface components to account for natural correlations that exist between these parameters. The MiRS uses the community RT model (CRTM) [26], [27] as the forward and adjoint operator. The CRTM is able to simulate the multiple scattering effects due to ice, rain, snow, graupel, and CLW at all microwave frequencies and is able to generate the corresponding Jacobians for all atmospheric and surface parameters. The CRTM is valid in clear, cloudy, and precipitating conditions. In the MiRS, the radiances are bias corrected before being ingested to the system. This correction removes potential inconsistencies between measurements and simulated brightness temperatures. The simulated radiances in this case use the CRTM forward model and inputs from the European Centre for Medium-Range Weather Forecasts global analyses, interpolated in time and space to the specific locations of the measurements.

After the 1-DVAR step is performed, a number of primary products are generated. Those products are the surface (skin temperature and emissivity spectrum), atmospheric (temperature and humidity profile), cloud, and hydrometeor (rain and ice water profiles) parameters that most directly impact the brightness temperatures. These MiRS core products are translated into derived products via the following two mechanisms: 1) a vertical integration procedure, which is used to derive products such as the total precipitable water, CLWP, RWP, and IWP and 2) the postprocessing procedures, which are used to generate the sea-ice concentration over sea ice, snow water equivalent over snow-covered land from the emissivity spectrum, and

TABLE I
COMPARISON BETWEEN THE RAINFALL RATE ESTIMATED FROM A REGRESSION TECHNIQUE AND THE RAINFALL RATE REFERENCE USED FOR THE TRAINING OF THE ESTIMATED RAINFALL RATE

Rain Comparison	Correlation	Bias (mm/h)	RMSE (mm/h)	Number of Points	Surface	Predictors used in the Regression
Regressed Rain Rate vs MSPPS Rain Rate	0.851	$-6.41\text{x}10^{-9}$	1.02	4871	Land	RWP and IWP
Regressed Rain Rate vs MM5 Rain Rate	0.887	$-5.72\text{x}10^{-6}$	4.542	41837	Ocean	RWP, IWP and CLWP

surface rainfall rate from the retrieved hydrometeor amounts. With respect to the hydrometeors over the ocean, the MiRS geophysical products are retrieved using two attempts of the inversion process. Over the ocean, the first attempt assumes that there are no absorption or scattering effects of larger hydrometeors (i.e., RWP and IWP), with CLW as the only retrievable hydrometeor. The second attempt, which is performed only in the case of nonconvergence of the first attempt, assumes precipitating conditions (with rain and ice) but with no CLW. Over land, due to the lower radiometric sensitivity to hydrometeors over the higher emissivity surface, CLW is not retrieved, with RWP and IWP added during the second attempt.

C. Description of the MiRS Rainfall Rate Postprocessing Technique

The MiRS rainfall rate postprocessing is a precipitation estimation technique based on the MiRS hydrometeor products, including CLW, ice water, and RWP. The MiRS precipitation estimation technique takes advantage of the physical relationship found between atmospheric hydrometeor amounts and surface rainfall rate. Previous work has reported the use of a relationship between IWP and surface rain rate to derive surface precipitation fields over ocean and land surfaces [4], [28]. As presented in (3), the rainfall rate technique presented in this paper uses a multilinear regression approach that requires CLWP, IWP, and RWP (given in millimeters) and a set of regression coefficients corresponding to each hydrometeor in order to retrieve the instantaneous rainfall rate (in millimeters per hour). During the development of the proposed technique, it was found that RWP and IWP were the two hydrometeors that maintained the largest correlation with respect to the surface rain rate. In essence, the MiRS precipitation technique estimates the surface rainfall rate by capturing signatures from both energy emitted (and scattered in the case of rain) by cloud liquid and raindrops (through the use of CLWP and RWP) and energy mainly scattered by ice particles (by means of the IWP)

$$RR = a_0 + a_1\text{CLWP} + a_2\text{RWP} + a_3\text{IWP}. \tag{3}$$

In (3), RR is the estimated surface precipitation (given in millimeters per hour), and a_0, a_1, a_2, and a_3 are a set of predefined regression coefficients. The regression coefficients are static components in the relationship presented in (3). Those coefficients have been determined based on an offline training using collocated sets of rainfall rate and hydrometeors both coming from the fifth-generation Pennsylvania State University and the National Center for Atmospheric Research Mesoscale Model (MM5) [29] data for the ocean surface type. For the land surface type, the regression coefficients have been derived using the surface rainfall rate retrieved by the operational Microwave Surface and Precipitation Products System (MSPPS) [4] and the hydrometeors retrieved by the MiRS. For the computation of the regression coefficients, precipitation cases during the warm and winter seasons were selected in order to provide information over different seasons to the regression coefficients. For the evaluation of the estimated rainfall rate based on (3), statistical comparisons against the MM5 rainfall rate and MSPPS precipitation estimate were performed. Table I provides the statistical information about the quality of the estimated rainfall rates with respect to the precipitation references used during the training process.

As described in (4) and (5), two relationships are used to compute the MiRS surface rainfall rate over the ocean and land. From these equations, it is possible to observe that IWP has a significant contribution to the estimation of precipitation over land, while the RWP contribution is dominant over the ocean surface. Since the MiRS does not retrieve CLW over the land surfaces, only RWP and IWP were used as predictors to estimate the surface rainfall rate over land

$$RR_{\text{ocean}} = 0.274 + 2.202\ \text{CLWP} + 5.329\ \text{RWP} - 0.302\ \text{IWP} \tag{4}$$

$$RR_{\text{land}} = -0.0264 + 9.742\ \text{RWP} + 12.036\ \text{IWP}. \tag{5}$$

The MiRS rainfall rate is only computed if the RWP and IWP are greater than 0.005 mm. For the ocean case, a CLWP threshold of 0.275 mm is being used to determine the presence of precipitation. This result is in agreement with the threshold values reported in [30].

In this paper, the hydrometeors retrieved by the MiRS are used to estimate the surface rainfall rate. Therefore, the quality of the estimated rainfall rate is primarily determined by the quality of the MiRS hydrometeor products, which, in turn, depends on the information content of the measurements. With respect to the quality of the MM5 rainfall rate and MSPPS precipitation estimate that were used to compute the regression coefficients of (4) and (5), results have been reported in previous studies. For example, in [31] and [32], the precipitation forecast

skill of the MM5 has been evaluated against the rain gauge observations over different seasons, showing bias score values close to one and root-mean-square error (rmse) values ranging from 12 to 25 mm for light precipitation thresholds (3–25 mm) and from 25 to 50 mm for moderate precipitation thresholds (25–50 mm). In addition, studies over convective environments presented in [33] have shown the ability of MM5 to simulate the evolution of convective precipitation, with errors on the order of 1.0 mm/h or less when compared with the rain-gauge-based observations. In the case of the MSPPS precipitation, 48-h comparisons against the Stage IV rainfall product (radar and rain gauge composite) demonstrate that the MSPPS precipitation can achieve a correlation of about 0.8 [4]. In the same study, monthly rainfall comparisons against rain gauge observations over Australia report a correlation of nearly 0.9, a mean absolute error of 65.2 mm, and an rmse value of 89.0 mm.

In the next section, an assessment of the MiRS rainfall rate estimate using a set of different precipitation references over different time scales is presented. Since the MiRS precipitation estimation technique is based on a relationship between hydrometeors, evaluating the quality of the MiRS precipitation estimate is also an indirect method that is used to evaluate the quality of the hydrometeors retrieved by the MiRS (a more direct evaluation in terms of probability distributions is presented in Section IV-E).

IV. Assessment of the Precipitation Estimation Technique

Precipitation is one of the most difficult parameters to assess due to the lack of a precipitation standard reference. In order to assess the performance of the rainfall rate estimation technique presented in this paper, extensive comparisons with respect to precipitation products derived from rain gauges, combined rain gauge and radar observations, and satellite-based microwave observations have been carried out over the ocean and land surfaces. Since the developed precipitation technique depends on the hydrometeor products derived by the MiRS system and since it is actually embedded as part of this system, the precipitation technique presented in this paper will be referred to as the MiRS rainfall rate estimation algorithm or technique. The assessment of the MiRS rainfall rate estimation algorithm is primarily performed through comparisons with the following: 1) the hourly National Centers for Environmental Prediction (NCEP) Stage IV precipitation that uses combined rain gauge and radar observations; 2) the instantaneous rainfall rate derived from the satellite-based TRMM-2A12 precipitation product; 3) the daily precipitation composites derived from rain gauge and radar observations as part of the external and independent validation performed by the IPWG; 4) the Operational Microwave Surface and Precipitation System (MSPPS) rainfall rate product; and 5) the frequency distribution histograms of TRMM-2A12 and the Weather Research Forecast (WRF) model rainfall rate.

The MiRS precipitation estimation algorithm is an operational algorithm that has been applied to AMSU and MHS sensors onboard NOAA-18, NOAA-19, and Metop-A, as well as to SSMI/S onboard DMSP-F16 and DMSP-F18. For the NOAA-18, NOAA-19, and Metop-A cases, the precipitation estimates are being produced at the AMSU-A resolution (approximately 50 km at nadir) [34], while for the DMSP-F16 and DMSP-F18 cases, the MiRS precipitation products are being generated at the Upper Atmospheric Sounding channel resolution of about 75 km [35]. These spatial resolution differences, as well as the different temporal coverage and quality of the observations, must be accounted when comparing the performances of the MiRS precipitation estimation products, particularly for the results presented in Sections IV-A and B. Here, it is important to mention that the MiRS has the ability to produce precipitation estimates at higher resolutions, such as at MHS and SSMI/S Imaging channel resolutions (approximately 15 and 12.5 km, respectively), limited only by available computational resources.

A. Assessment Using the NCEP Stage IV Precipitation Product

The hourly NCEP Stage IV precipitation analysis has been used as a reference for the assessment and evaluation of the MiRS rainfall rate technique. Produced by the 12 River Forecast Centers over the Continental U.S. (CONUS), the NCEP Stage IV product is a 4-km resolution precipitation analysis derived from hourly radar precipitation estimates and hourly rain gauge data [36]. The Stage IV precipitation analysis product is much more of an integrated hourly estimate, while the satellite-based MiRS precipitation estimation products represent an instantaneous observation. Because of that, during the comparison, it has been assumed that the Stage IV rainfall rate is a constant amount for an entire hour and is compared with the MiRS precipitation estimates that had occurred within that hour. The comparison has been carried out over all satellite-based sensors where the MiRS precipitation technique has been applied operationally. Comparisons between the Stage IV precipitation analysis and MiRS precipitation estimates have been performed over land surfaces since late October 2009. Results corresponding to the MiRS DMSP-F18 precipitation estimate are only valid after the beginning of March 2010, which is the time when DMSP-F18 observations became available. Fig. 1 shows the performance of the MiRS precipitation estimation products based on daily time–space matchups with the Stage IV precipitation analysis product, observed from the end of August 2009 to May 2010. In this comparison, the time and space collocation thresholds were set to 3 min and 25 km, respectively, for the NOAA-18, NOAA-19, and Metop-A AMSU/MHS cases and 3 min and 37.5 km for the DMSP-F16 and DMSP-F18 SSMI/S cases. During the collocation procedure, the collocated Stage IV pixels were averaged within the satellite footprint. Statistics were computed for ten-day periods in order to result in reasonably stable statistics. In addition, the time series of the probability of detection, false alarm rate and Heidke skill score have been produced using a precipitation threshold of 0.5 mm/h. For the computation of the bias, correlation and rmse, values of rainfall rate equal to zero mm/h were included.

When analyzing the bias values in Fig. 1(a), it is clear that all of the MiRS precipitation products consistently have values

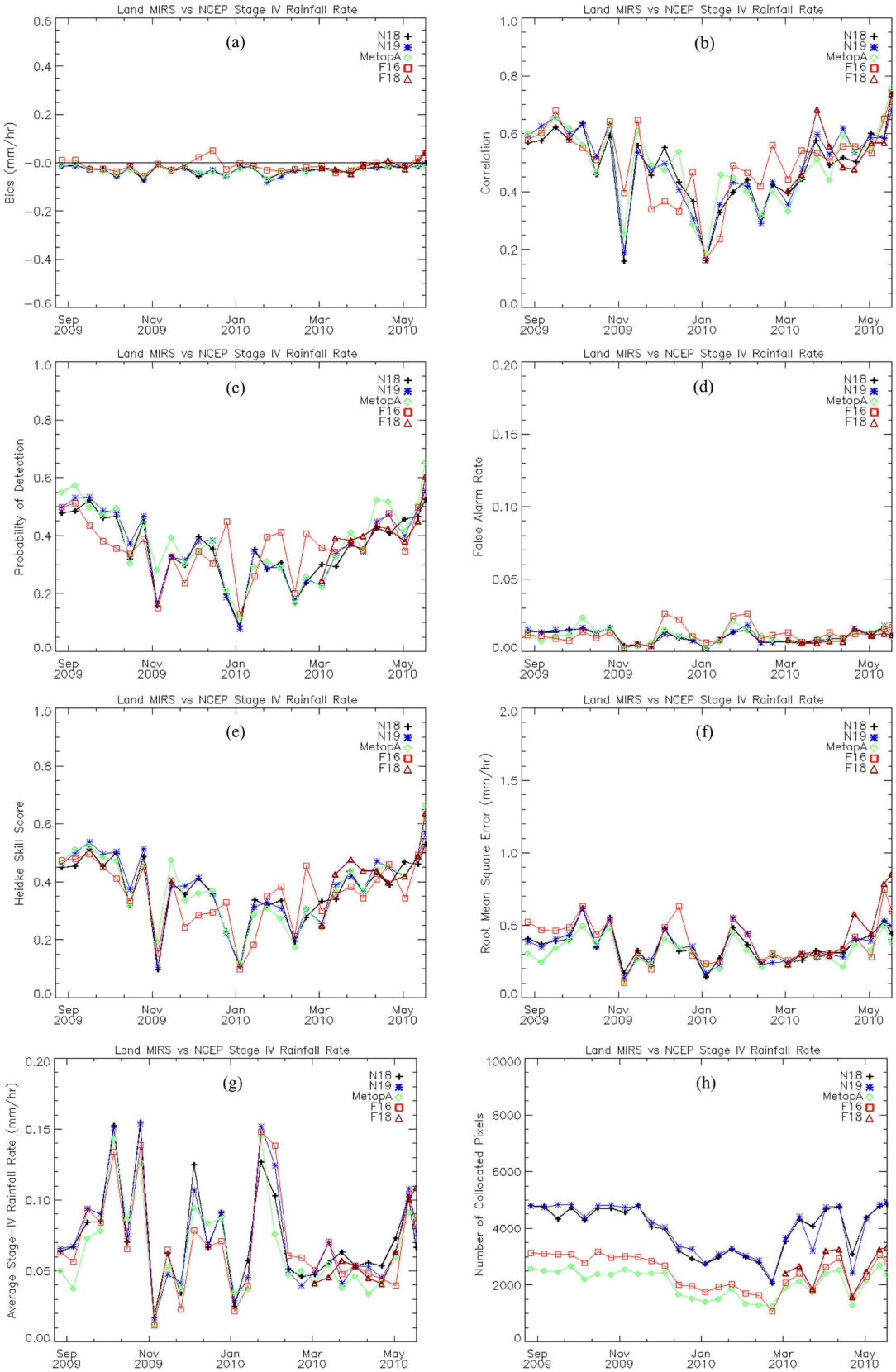

Fig. 1. Time series of the (a) bias, (b) correlation, (c) probability of detection, (d) false alarm rate, (e) Heidke skill score, (f) rmse, (g) average of the observed Stage IV rainfall rate, and (h) number of collocated pixels computed over ten-day periods for MiRS precipitation estimation products, including NOAA-18 (N18), NOAA-19 (N19), Metop-A, DMSP-F16 (F16), and DMSP-F18 (F18), when compared against the NCEP Stage IV precipitation product.

close to zero (a positive bias denotes that the precipitation estimation product is greater than the precipitation reference), with a typical variation that is no larger than ± 0.05 mm/h. The bias results reported in Fig. 1(a) show that, most of the time, the MiRS precipitation products detect slightly lower precipitation values than the values of the Stage IV precipitation. In terms of correlation, different performances are observed during the comparison period, as shown in Fig. 1(b). For example, before November 2009, correlation values above 0.55 are observed. However, after November 2009 and before April 2009, the correlation values range from 0.30 to 0.50, having minimum values at the beginning of both November 2009 and January 2010. Moreover, approximately after April 2010, the correlation has consistently increased to values above 0.50. Based on these results, it can be noted that the lowest correlations in the MiRS precipitation products occur during the winter season, and larger correlation values are observed during the warm season.

With respect to the contingency-table-based probability of detection (which measures the fraction of observed precipitation events as defined by the reference that were detected correctly) shown in Fig. 1(c), similar variations to those observed for correlation have been detected. For example, before November 2009 and after April 2010, the probability of detection shows a good performance, with values typically larger than 0.40. On the other hand, values of probability of detection varying between 0.20 and 0.40 are observed between November 2009 and March 2010. In addition to the probability of detection, we analyze the false alarm rate which provides insight about the fraction of retrieved precipitation events that were incorrect (no precipitation as defined by the reference). By observing the time series of the false alarm rate in Fig. 1(d), it is noted that, over the entire comparison period, among the cases where the Stage IV precipitation product observes nonprecipitation conditions, the MiRS estimates rainy conditions in less than 2%. We also compute the Heidke skill score or fraction of correct forecasts after eliminating those forecasts, which would be correct due purely to random chance. In Fig. 1(e), it is observed that the lowest performance of the precipitation estimates occurs during the November 2009 and March 2010 period (winter season), but an improvement is observed before November 2009 and after April 2010, with values above 0.40.

Analyzing the average magnitude of the forecast errors, by observing the rmse in Fig. 1(f), those results let us see that the lowest values of rmse occur near the beginning of November 2009 and January 2010, which are the periods when the correlation, probability of detection, false alarm rate, and Heidke skill score report the lowest performance. During the comparison period, the MiRS rainfall rate estimation products report similar rmse values, with variations varying from 0.10 to 0.60 mm/h. For reference purposes, the average of the Stage IV rainfall rate is also shown in Fig. 1(g). From this result, it is possible to identify that, in general, the lowest performance of the MiRS precipitation technique occurs when the lowest amount of precipitation is observed by the Stage IV precipitation product. Similar to other satellite-based precipitation estimation techniques, the MiRS precipitation estimation technique has difficulties in detecting low amounts of rainfall over land, which is commonly found during the winter season and is typically associated with nonconvective low level clouds. In addition, a strong correlation between the rmse value and the averaged observed precipitation from Stage IV is found. The larger the averaged observed precipitation is, the bigger is the rmse value. This result is in line with the results reported in [37], where a study about the expected root-mean-square random error associated with the space–time average precipitation estimates is reported. In Fig. 1(h), the number of collocation pixels associated with each of the MiRS precipitation estimation products is also presented. The number of time–space matchups found is typically larger than 2000. From this result, no clear relationship is observed between the number of time–space matchups and the performance of the MiRS precipitation products.

The results reported in Fig. 1 have shown that the MiRS precipitation estimation technique performed better during the warm season than during the cool season. These results are in agreement with previous studies that have demonstrated the higher performance of the satellite-based microwave precipitation estimates during the summer season [18]. With respect to the individual performance of the five MiRS precipitation products evaluated in this section, it is observed that no single precipitation product consistently outperforms any other. Although the MiRS precipitation estimation products used in this comparison have been derived from observations performed with different microwave sensors, it is remarkable to note the similarity in their performances, particularly those precipitation products that have similar spatial resolution. These results are important and establish confidence as to the applicability of the MiRS precipitation estimation algorithm on multiple satellite-based microwave sensors, without degrading the quality of the precipitation product.

B. Assessment Using the TRMM-2A12 Precipitation Product

The TRMM-2A12 surface rainfall product is a mature precipitation product that relies on observations from the TRMM Microwave Imager (TMI) sensor [1]. The generation of the TRMM-2A12 precipitation, which is given in millimeters per hour, is based on an algorithm that uses a Bayesian approach to match the observed multichannel brightness temperatures to the simulated hydrometeors provided in a preexisting database. Since mid-September 2009, time and space collocations between the TRMM-2A12 version 6.0 precipitation and the MiRS precipitation products, including NOAA-18, NOAA-19, Metop-A, DMSP-F16, and DMSP-F18, have been performed on a daily basis. For the comparisons, 3 min and 25 km were used as the time and space collocation thresholds, respectively, for the NOAA-18, NOAA-19, and Metop-A AMSU/MHS cases. For the F16 and F18 SSMI/S, 3 min and 37.5 km were used as the time and space collocation thresholds. Fig. 2 shows the performance of the MiRS precipitation estimation products when the satellite-derived TRMM-2A12 rainfall product is used as a precipitation reference. The comparisons presented here have been carried out mainly over ocean surfaces. One difference with respect to the NCEP Stage IV comparison presented in the previous section is that both the TRMM-2A12 and MIRS precipitation products correspond to instantaneous

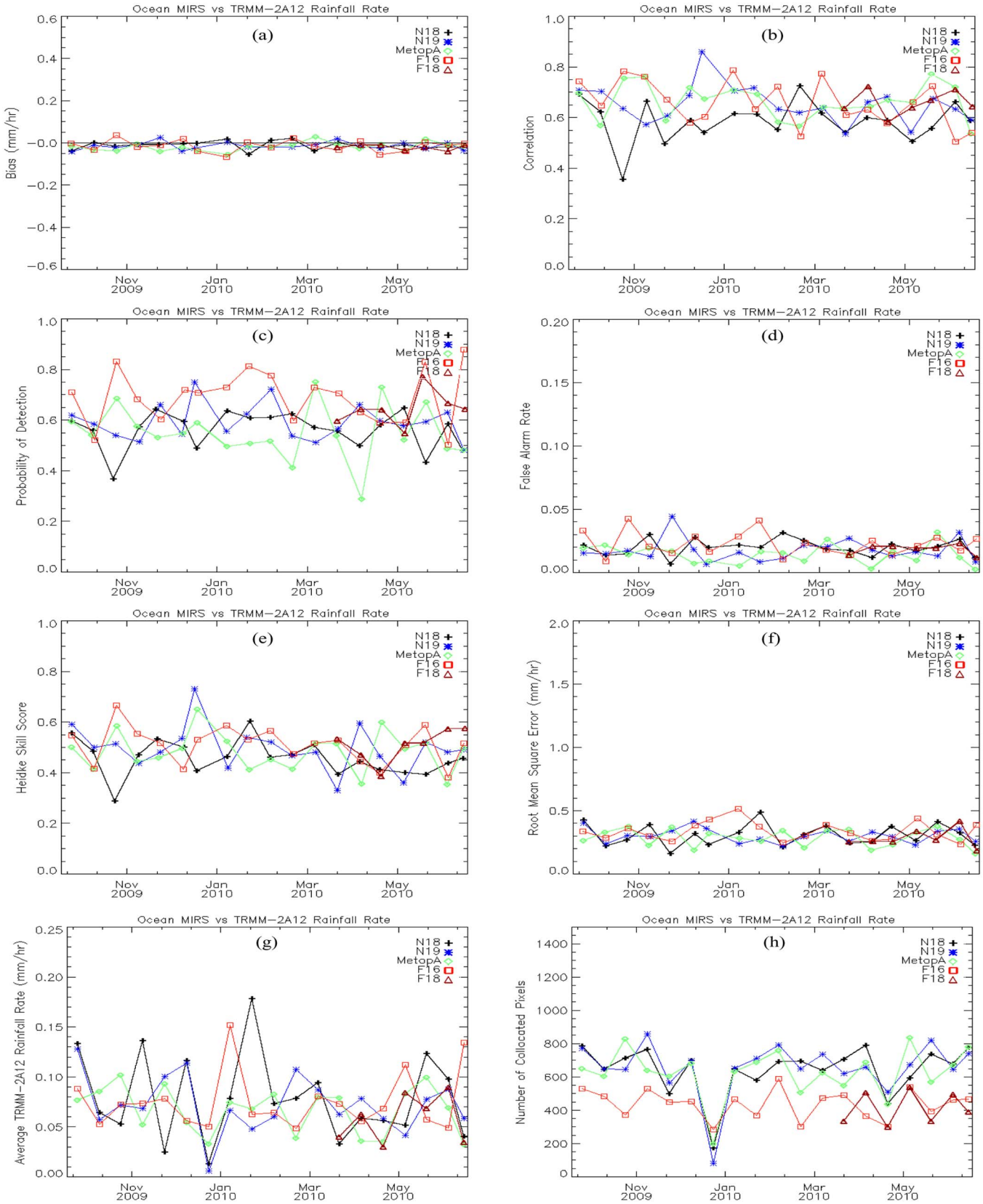

Fig. 2. Time series of the (a) bias, (b) correlation, (c) probability of detection, (d) false alarm rate, (e) Heidke skill score, (f) rmse, (g) average of the observed TRMM-2A12 rainfall rate, and (h) number of collocated pixels computed over 15-day periods for the MiRS precipitation estimation products, including NOAA-18 (N18), NOAA-19 (N19), Metop-A, DMSP-F16 (F16), and DMSP-F18 (F18), when compared against the TRMM-2A12 surface rainfall rate over the ocean.

observations. Time–space matchups were not found regularly from day to day. This, along with the intrinsic variability of precipitation, tends to generate large variability in the computed statistics. In order to generate more stable statistics, comparisons were performed for 15-day periods. The time series of the probability of detection, false alarm rate and Heidke skill score shown in Fig. 2 have been produced using a precipitation threshold of 0.5 mm/h. On the other hand, values of rainfall rate equal to zero mm/h were accounted for the computation of the bias, correlation and rmse. The MiRS DMSP-F18 precipitation product has been the most recent precipitation product generated using the MiRS rainfall rate algorithm. Because of that, the MiRS DMSP-F18 precipitation was included in this assessment just after mid-March 2009, as shown in Fig. 2.

In Fig. 2, the performance of the MiRS precipitation products against the TRMM-2A12 rainfall rate is reported. Bias values about zero are observed over the entire comparison period, as shown in Fig. 2(a). The variability of the bias typically oscillates between ± 0.05 mm/h. With respect to the correlation performance shown in Fig. 2(b), values from 0.60 to 0.80 are commonly found for all MiRS precipitation estimates. These results suggest a strong relationship between the TRMM-2A12 and the MiRS rainfall rate. Close to the beginning of November 2009, the MiRS NOAA-18 precipitation shows a low correlation of about 0.35. Apart from this case, the MiRS NOAA-18 precipitation has shown correlation values near 0.60. In the case of the time series of probability of detection shown in Fig. 2(c), we can observe that most of the MiRS precipitation products have values varying from 0.60 to 0.80. The lowest probabilities of detection observed in Fig. 2(c) correspond to the MiRS NOAA-18 precipitation occurring close to the beginning of November 2009, with a value of about 0.35, and to the MiRS Metop-A, found near the beginning of April 2010, with a value of about 0.30. The MiRS Metop-A precipitation shows the higher variability in the probability of detection, particularly during March 2010 to April 2010, which corresponds approximately to the transition between the cool and warm seasons. Apart from that, no clear seasonal dependence is observed in the probability of detection performance, while similar detection capabilities are found among the MiRS precipitation estimation products. In principle, no significant seasonal dependence is expected in the performance of the MiRS precipitation estimation products since the comparison is being performed mainly over the tropical oceans.

With respect to the false alarm rate performance reported in Fig. 2(d), the MiRS precipitation products show similar false alarm rate values, generally below 0.03. This indicates that the MiRS precipitation estimation algorithm forecasts rainy conditions in less than 3% over regions where the TRMM-2A12 precipitation product observes no precipitation. In Fig. 2(e), the Heidke skill score results clearly show similar capabilities of the MiRS precipitation products to correctly detect rainy conditions. Typical Heidke skill scores are found to be between 0.40 and 0.60. The lowest Heidke skill score values correspond to the MiRS NOAA-18 occurring close to the beginning of November 2009. The rmse values reported in Fig. 2(f) show that the average errors of the MiRS precipitation estimates are about 0.30 mm/h. By observing the average rainfall rate of the TRMM-2A12 precipitation product shown in Fig. 2(g), larger values of rmse are related to larger values of average TRMM-2A12 rainfall rate. This result is similar to the one observed in the assessment presented in Section IV-A, where Stage IV precipitation was used as the precipitation reference. In addition, a low performance of the MiRS precipitation products is also found when low rainfall rates are observed. On the other hand, the number of time–space matchups is shown in Fig. 2(h). This result shows that typically more than 400 time–space matchups were found during the comparison period.

The results presented in this section show that the five MiRS precipitation estimation products compare favorably with respect to the TRMM-2A12 precipitation product over the ocean. It has been observed that the various MiRS precipitation estimation products have all shown similar performance when using the TRMM-2A12 precipitation product as a precipitation reference. This result is relevant when considering that the MiRS precipitation estimation products are derived from different satellite-based microwave sensors. The better performance of the MiRS precipitation technique found in this section with respect to the results presented in Section IV-A (over land assessment using NCEP Stage IV) is related to the larger brightness temperature contrast between precipitating and nonprecipitating conditions observed at the microwave emission channels over the ocean than the contrast observed over the land surfaces. However, the fact that the comparison with respect to the Stage IV precipitation is based on the assumption that rainfall rates are constant for an hour must be accounted when comparing the results reported in this section and Section IV-A.

From the comparisons against both the Stage IV precipitation (presented in previous section) and TRMM-2A12 precipitation products, the MiRS DMSP-F18 precipitation estimation product has consistently shown a good performance. A noteworthy aspect of this MiRS precipitation estimation product is that, just a few weeks after the DSMP-F18 data became available, the MiRS DMSP-F18 precipitation estimation product was generated on a daily basis. Recently, this precipitation product was elevated to operational status due to the good quality observed when compared to well-known precipitation references, including rain gauges, rain radars, and satellite-based precipitation products. This result demonstrates the capability of the MiRS precipitation estimation algorithm to be applied operationally in a relatively short period of time while maintaining a high-quality performance.

C. Assessment as Part of the IPWG Validation/Intercomparison

For assessment purposes, the MiRS precipitation composite estimate given in millimeters per day has been generated using the rainfall rate samples (given in millimeters per hour) from three MiRS precipitation estimation products: MiRS NOAA-18, Metop-A, and DMSP-F16. Computed from -60° to 60° latitudes and with a spatial resolution of 0.25°, the daily MiRS precipitation composite has been included as part of the IPWG validation/intercomparison. The IPWG is dedicated to perform large-scale validations

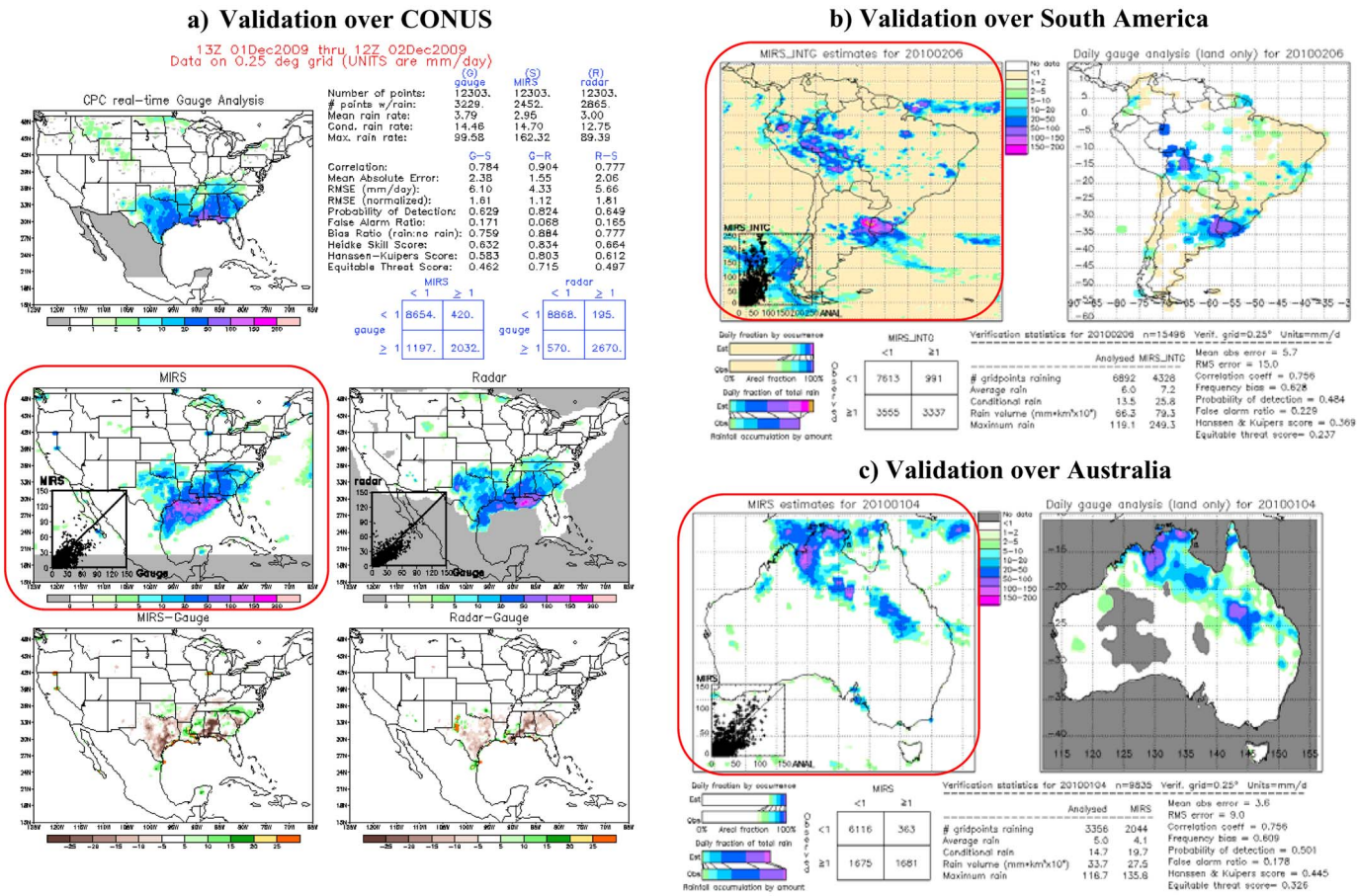

Fig. 3. (a) CONUS, (b) South American, and (c) Australian regions where the MiRS rainfall estimation algorithm is being validated as part of the IPWG validation/intercomparison. Red rectangles enclose the daily MIRS precipitation composite estimate given in millimeters per day. The images of the validation over CONUS, South America, and Australia are courtesy of John Janowiak from the University of Maryland, College Park, Daniel Vila from the Instituto Nacional de Pesquisas Espaciais, Brazil, and Elizabeth E. Ebert from the Bureau of Meteorology, Australia, respectively.

and intercomparisons of daily rainfall estimates from operational and semioperational satellite precipitation estimates against "ground truth" precipitation references based on the rain gauge and/or ground-based radar observations. More information about the IPWG validation/intercomparison can be found at http://cawcr.gov.au/projects/SatRainVal/validation-intercomparison.html.

The IPWG validation/intercomparison has helped algorithm developers in understanding the strengths and weaknesses of the satellite rainfall algorithms, as well as in contributing to their improvement by evaluating the performance of the algorithms on a daily basis over a wide range of weather and climate regimes. The IPWG performs validations of satellite precipitation estimates over Australia, CONUS, South America, Europe, and Japan. Currently, the daily MiRS precipitation composite estimate is being validated over CONUS, South America, and Australia, and its incorporation to other regions is in progress. For the validation over CONUS and South America, the daily MiRS precipitation composite estimate extends from 12:00 UTC to 12:00 UTC, while for the validation over Australia, the MiRS composite extends from 00:00 UTC to 24:00 UTC.

The validation of the precipitation estimates as part of the IPWG validation/intercomparison is based on both quantitative and qualitative comparisons. The qualitative comparisons are performed using maps that allow the evaluation of the satellite rainfall estimates on a case by case basis. Statistics, as well as contingency tables, which contain counts of zeros (no rain analyzed or estimated), false alarms, misses, and hits, are used to perform quantitative comparisons. Examples of the statistics generated as part of the IPWG validation include rmse, correlation, probability of detection, and Heidke skill score. These parameters are used to perform a more complete analysis of the capabilities of the precipitation estimation algorithms. Fig. 3 shows an example of the qualitative and quantitative validation of the MiRS precipitation that is being carried out at the IPWG on a daily basis. As identified in Fig. 3(a), the validation over the CONUS region is being performed using both rain gauge analysis and radar observations. On the other hand, over South America and Australia, only rain gauge analysis is being used for the validation. Over South America, low spatial coverage of the rain gauge analysis has been identified particularly over the Amazon rainforest region, south of Argentina, and Chile. From the table found in the CONUS validation image, shown at the upper right side of Fig. 3(a), the columns identified as G-S and R-S summarize the daily quantitative comparison between the MiRS precipitation composite and the precipitation derived from both rain gauge measurements and

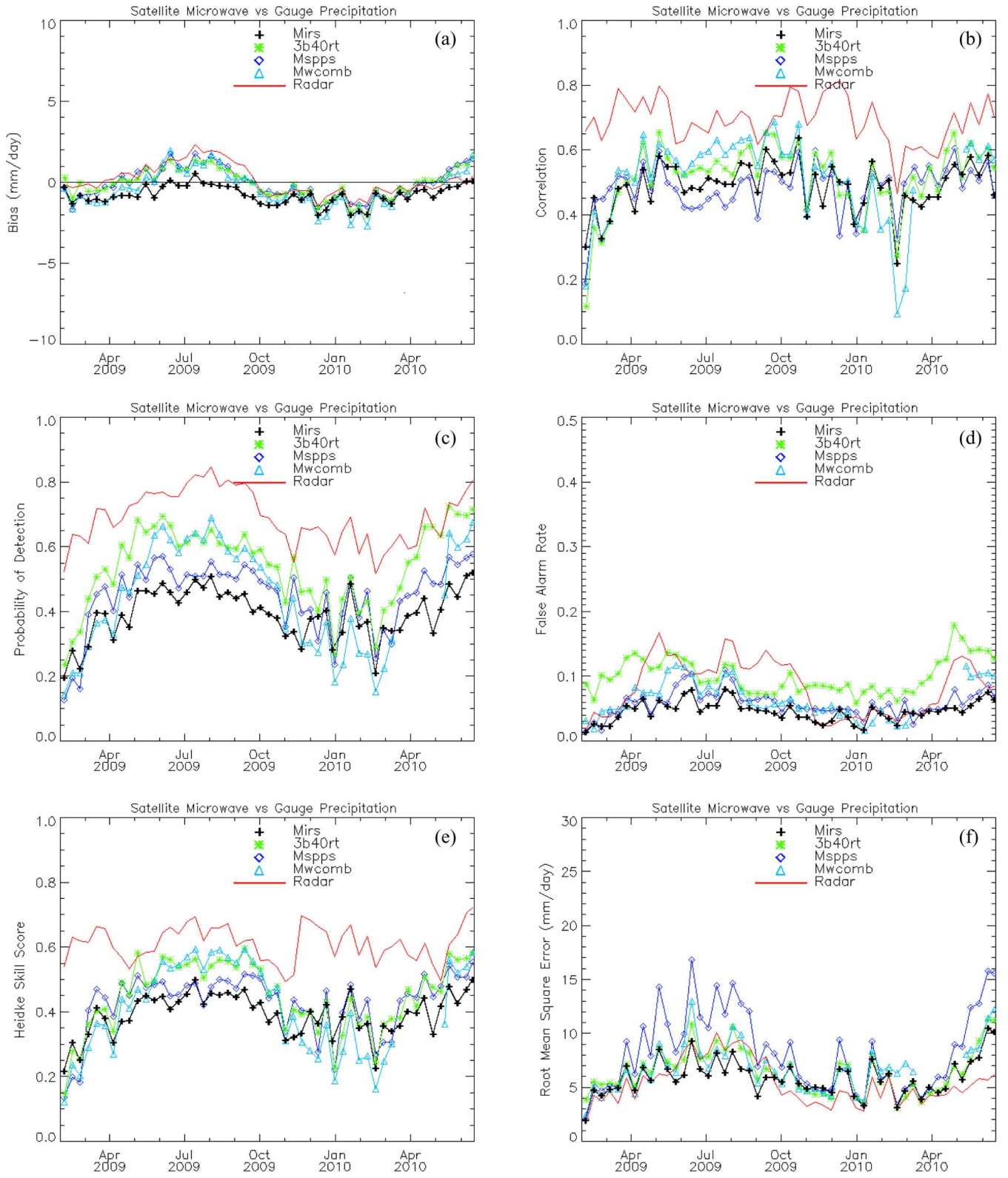

Fig. 4. Time series of the (a) bias, (b) correlation, (c) probability of detection, (d) false alarm rate, (e) Heidke skill score, and (f) rmse for the MiRS, 3B40RT, MSPPS, and MWCOMB precipitation estimation products, as well as rain radar, when compared against the rain gauge observations over the CONUS region as part of the IPWG validation/intercomparison. The time series of the statistics is computed over ten-day periods.

ground-based radar observations, respectively. Similar quantitative comparisons are observed over the South America and Australia validation images. From the three images of the MiRS precipitation shown in Fig. 3, it is possible to identify that the MiRS precipitation estimation algorithm is capable of retrieving precipitation with no discontinuities at the coasts. This is

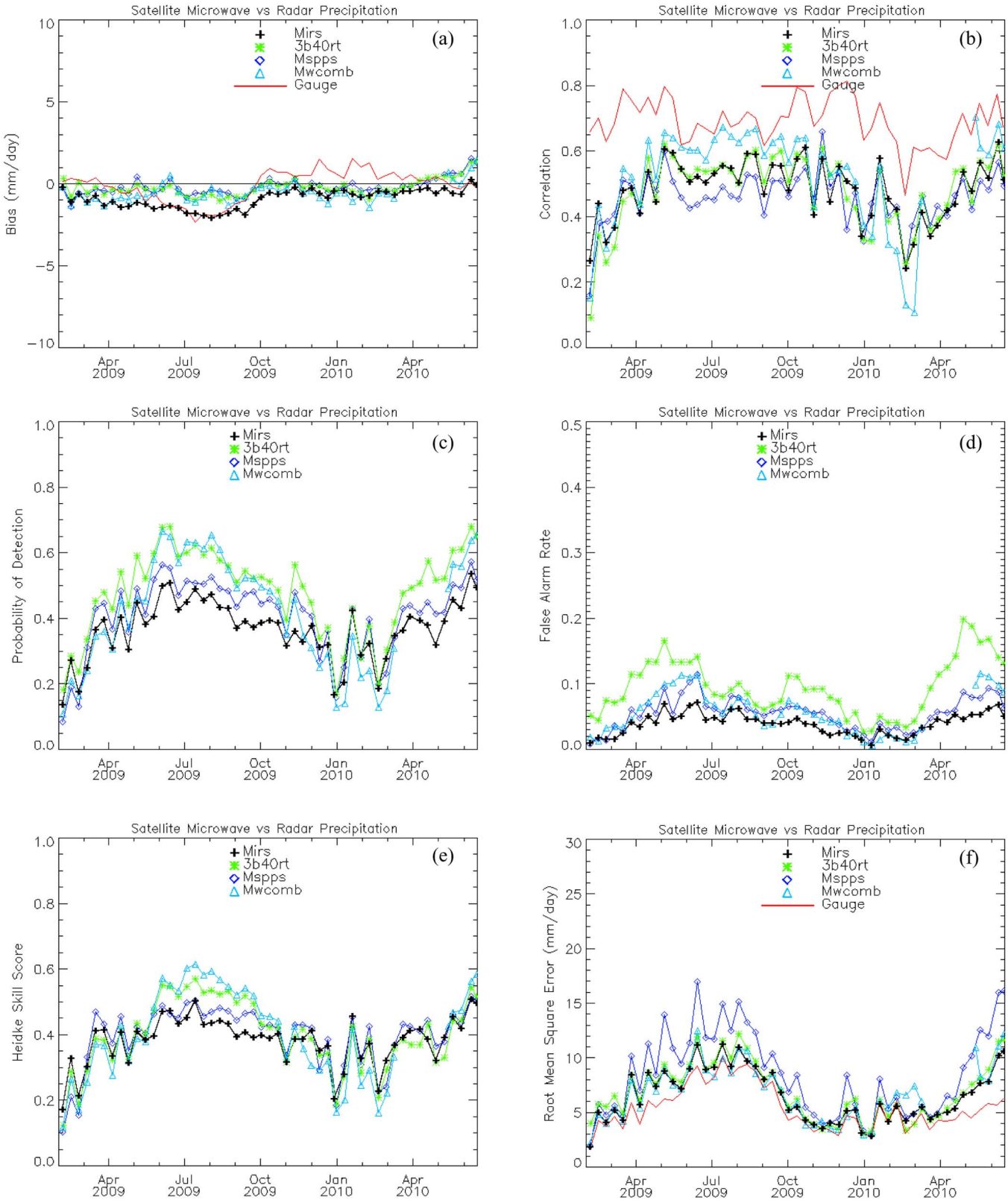

Fig. 5. Time series of the (a) bias, (b) correlation, (c) probability of detection, (d) false alarm rate, (e) Heidke skill score, and (f) rmse for the MiRS, 3B40RT, MSPPS, and MWCOMB precipitation estimation products, as well as rain gauge, when compared against the rain radar observations over the CONUS region as part of the IPWG validation/intercomparison. The time series of the statistics is computed over ten-day periods.

a property of the MiRS precipitation estimation algorithm that has been consistently observed throughout the evaluation of the algorithm.

In order to analyze the performance of the MiRS precipitation estimation algorithm over different latitudes and seasons, the time series of the statistics has been generated over several

TABLE II
SATELLITE-BASED MICROWAVE PRECIPITATION ESTIMATION ALGORITHMS VALIDATED AS PART OF THE IPWG VALIDATION/INTERCOMPARISON

Satellite-based Microwave Precipitation Estimation Algorithm	Responsible Organization	No. of Sensors	Satellites/Instruments	Description
MiRS	NOAA/NESDIS/STAR	3	NOAA-18, Metop-A (AMSU-A and MHS) and F16-SSMIS	A sensor independent, physical-based and regression-based algorithm that depends on MiRS RWP, IWP and CLWP as predictors.
MSPPS	NOAA/NESDIS/STAR	2	NOAA-18 and Metop-A (AMSU-A and MHS)	Rain rate is computed based on an IWP and rain rate relationship [4], where IWP is retrieved by MSPPS.
3B40RT	NASA	4	TRMM (TMI), F13, F14 and F15 (SSM/I)	Provides a merger of all available SSM/I and TMI microwave precipitation estimates into a high-quality estimate [11].
MWCOMB	CPC	8	TRMM (TMI), F13, 14, 15 (SSM/I), NOAA-15, 16, 17 (AMSU-B) and 18 (MHS)	Precipitation estimates are daily composites of precipitation estimates from SSM/I, AMSU-B and TMI [9].

months and regions. Figs. 4 and 5 show the time series of the statistics generated from the validation performed over the CONUS region using rain gauges and rain radar observations as ground "truth" precipitation references. For comparison purposes, in Figs. 4 and 5, the performance of other satellite-based microwave precipitation estimation algorithms has been included. Information about the satellite-based microwave precipitation estimation algorithms shown in Figs. 4 and 5 is provided in Table II. Since nonvalid data from the MWCOMB algorithm were found from March 15 to May 13, 2010, no statistics are reported over this period in Figs. 4 and 5. At the IPWG validation/intercomparison, we have also had the opportunity to evaluate the performance of the MiRS precipitation algorithm over South America and Australia for several months. For the South American region, in addition to the MiRS precipitation estimation algorithm, the MSPPS precipitation algorithm is the other microwave-based algorithm that is being validated at the same time. Because of that, only the performance of these two precipitation algorithms will be analyzed. For the Australian region, the MWCOMB and 3B40RT algorithms (see Table II for additional information), as well as the MiRS and MSPPS algorithms, are the microwave-based precipitation estimation algorithms validated as part of the IPWG validation/intercomparison. The time series of the statistics derived from the validation performed over South America and Australia is shown in Figs. 6 and 7, respectively. All of the statistics shown in Figs. 4–7 have been generated using ten-day periods in order to generate stable statistics and with a precipitation threshold of 1.0 mm/day used for the computation of the probability of detection, false alarm rate, and Heidke skill score.

1) Assessment Over the CONUS Region: The first analysis starts with the evaluation of the results obtained over the CONUS region using Figs. 4 and 5. Based on more than one year of daily comparisons, Figs. 4(a) and 5(a) show that all microwave precipitation estimation algorithms have bias values close to zero, with a typical variation on the order of ± 2.0 mm/day. For the particular case of the MiRS precipitation algorithm, it shows bias values closer to zero, particularly during the May 2009 to September 2009 period, when the rain gauge is used as a precipitation reference [see Fig. 4(a)]. During the same time period, the other precipitation estimation algorithms show a better agreement with respect to the bias resulted from the gauge-radar comparison (solid line). However, when the radar-based precipitation is used as a reference [see Fig. 5(a)], the opposite result is observed. With respect to the correlation, reported in Figs. 4(b) and 5(b), all of the satellite-derived microwave precipitation algorithms have shown similar performance through the comparison period. However, the MWCOMB algorithm has shown higher correlation values during the May 2009 to October 2009 period (warm season), while the MSPPS precipitation algorithm has shown the lowest values during the same period. Moreover, for the same period of time, the MiRS and 3B40RT precipitation algorithms have reported correlation values in between the values reported by the MWCOMB and MSPPS precipitation algorithms. At this point, it is important to recognize the complexity associated with the evaluation of the satellite-based precipitation estimates when observing the statistics values generated from the rain gauge to rain radar comparison (solid lines in Figs. 4 and 5), which are two references commonly used as a ground "truth." For the particular case of correlation, we note that even the correlation values between these two ground references (rain gauge and rain radar) are rarely above 0.80 while having large variations going from 0.50 to 0.80. In our study, the statistics derived from the comparison between the rain gauge and rain radar observations establish an important reference about the performance of the precipitation estimation algorithms. For example, in the case of the probability of detection results shown in Figs. 4(c) and 5(c), the microwave precipitation

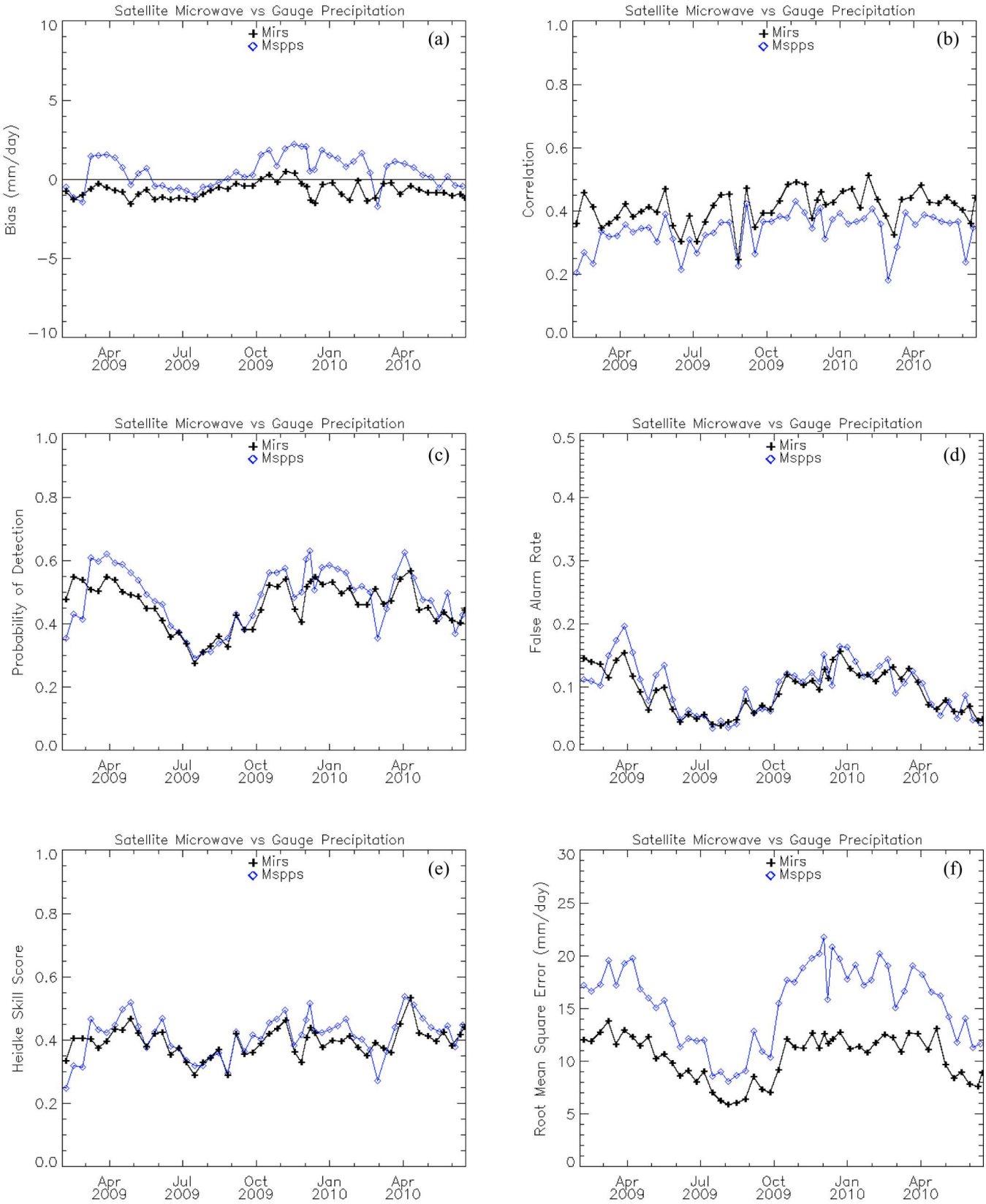

Fig. 6. Time series of the (a) bias, (b) correlation, (c) probability of detection, (d) false alarm rate, (e) Heidke skill score, and (f) rmse for the MiRS and MSPPS precipitation estimation products when compared against the rain gauge observations over South America as part of the IPWG validation/intercomparison. The time series of the statistics is computed over ten-day periods.

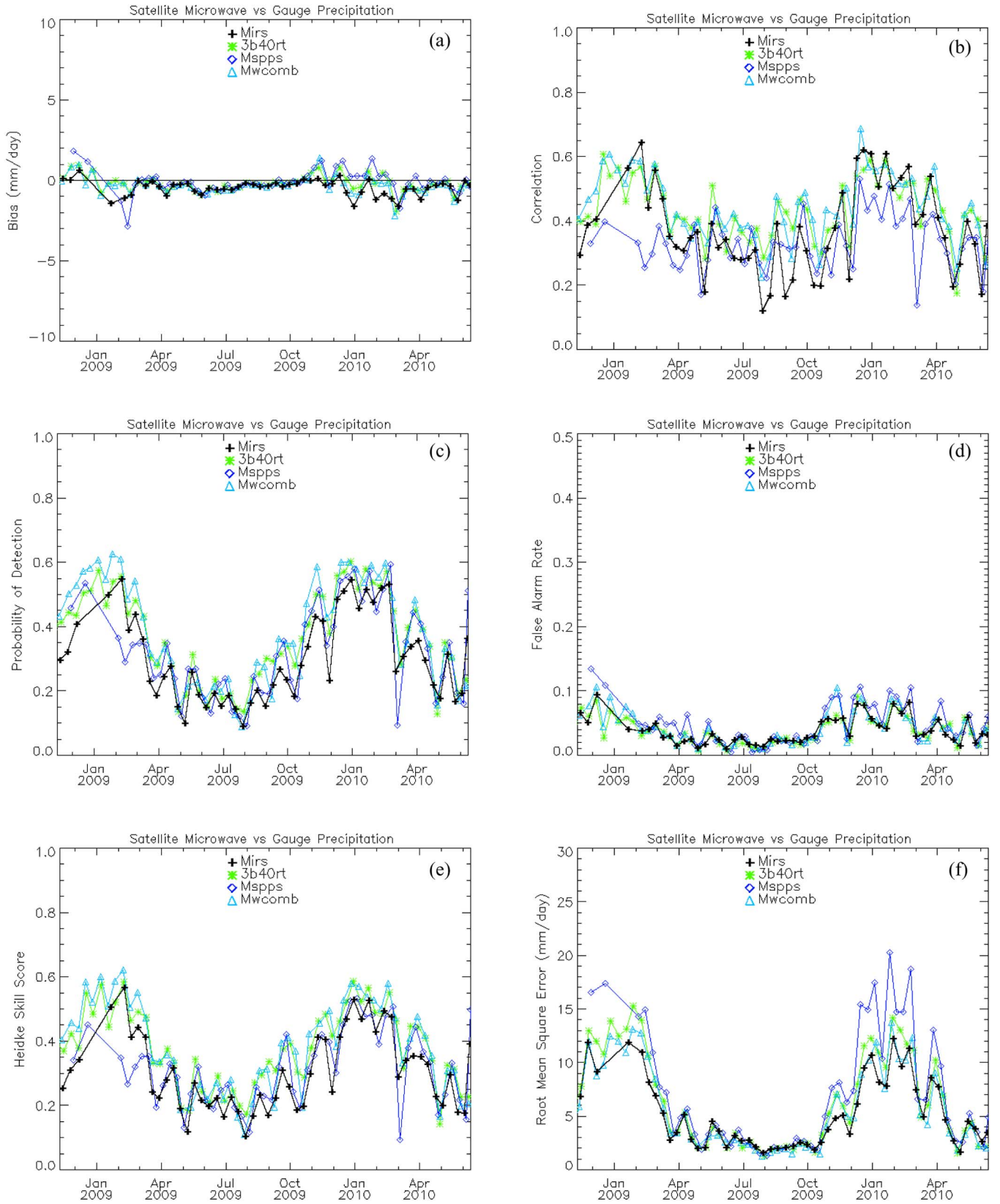

Fig. 7. Time series of the (a) bias, (b) correlation, (c) probability of detection, (d) false alarm rate, (e) Heidke skill score, and (f) rmse for the MiRS, 3B40RT, MSPPS, and MWCOMB precipitation estimation products when compared against the rain gauge observations over Australia as part of the IPWG validation/intercomparison. The time series of the statistics is computed over ten-day periods.

estimation algorithms have reported the larger probability of detection values during the May 2009 to October 2009 period or after May 2010, with values ranging from 0.45 to 0.65. However, the rain gauge to radar comparison shows that values of probability of detection ranging from 0.70 to 0.80 could be observed for the same period. Continuing our analysis, from the probability of detection results shown in Figs. 4(c) and 5(c), it has been observed that, during the May 2009 to October 2009 period (warm season), the 3B40RT and the MWCOMB precipitation algorithms have shown the best probability of detection, followed by the MSPPS and MiRS precipitation algorithms. The better performance of the probability of detection observed for the 3B40RT and MWCOMB precipitation algorithms is related to the larger temporal and spatial coverage associated with these algorithms, which, in turn, is due to the use of a larger number of sensors employed to generate the daily precipitation composites. As described in Table II, the 3B40RT and MWCOMB precipitation algorithms utilized four and eight microwave sensors, respectively, to generate the daily precipitation composites. On the other hand, the MSPPS and MiRS precipitation estimation algorithms use only two and three microwave sensors, respectively.

Another parameter that has been used to evaluate the performance of the microwave precipitation algorithms is the false alarm rate. The results found in Figs. 4(d) and 5(d) show that larger values of the false alarm rate are consistently observed for the 3B40RT precipitation algorithm, while the lowest values are observed for the MiRS precipitation algorithm, with values no larger than 0.07. This latter result in conjunction with the probability of detection results leads us to conclude that the precipitation estimation algorithms with the better capabilities to detect rainy conditions are also the ones that report larger false alarms. At the same time, when analyzing the Heidke skill score from the results shown in Figs. 4(e) and 5(e), it is observed that the MiRS precipitation algorithm performance is comparable to the other precipitation algorithms, particularly during the winter season. Finally, when analyzing the rmse values obtained during the comparison period shown in Figs. 4(f) and 5(f), it is observed that most of the precipitation algorithms, including the MiRS algorithm, have values varying from 2.0 to about 10.0 mm/day. Those values are in good agreement with respect to the rmse values corresponding to the rain gauge to rain radar comparison. On the other hand, the rmse values corresponding to the MSPPS precipitation estimation algorithm have consistently shown the largest rmse values, particularly over the April 2009 to October 2009 period and after April 2010, with values approximately varying from 10.0 to 15.0 mm/day.

2) Assessment Over the South American Region: The second region where the MiRS precipitation algorithm is being evaluated routinely is over South America. Over this region, the MSPPS precipitation algorithm is also being evaluated. From the results shown in Fig. 6(a), which are based on the daily comparisons performed for more than one year, it is possible to observe that bias values close to 0 mm/day have been reported, with the MiRS precipitation algorithm generally showing the closer values to 0 mm/day around April 2009, and from October 2009 to April 2010. On the other hand, with values varying from 0.30 to 0.50, the correlation of the MiRS precipitation has consistently shown larger values than the ones observed for the MSPPS precipitation, as reported in Fig. 6(b). It is important to notice that the correlation values reported over South America are slightly (0.1) less than the ones observed over the CONUS region. This is mainly related to the lower spatial coverage of the rain gauges deployed over South America, to the different rain gauge quality control considered over this region and to the different nature of precipitation regimes observed in South America with respect to the CONUS region.

For the probability of detection shown in Fig. 6(c), a clear seasonal dependence is observed by noticing that the lowest detection values occur during the June 2009 to August 2009 period (winter season), while the largest probabilities of detection occur about April 2009 and from October 2009 to April 2010 (warm season). From March 2009 to May 2009, the MSPPS algorithm has shown probabilities of detection larger than the ones observed for the MiRS algorithm by approximately 0.05. However, the results reported in Fig. 6(c) show that the MiRS and MSPPS precipitation algorithms have, in general, similar probability of detection, with the largest values being close to 0.60 and the lowest values near 0.30. With respect to the false alarm rate shown in Fig. 6(d), a seasonal dependence is also observed. For instance, the lowest false alarms occur during the winter season, while the largest false alarms occur during the warm season. The MiRS and MSPPS precipitation algorithms show very similar false alarm rate values that practically overlap one another. During the March 2009 to May 2009 period, the major false alarm differences are found, with the MiRS as the algorithm showing the lowest false alarms for this period. Notice that that this is the same period of time where the largest differences in the probability of detection have been detected. On the other hand, when comparing the false alarm rate values found over South America with respect to the ones obtained over CONUS, a difference of about 0.05 is observed, particularly over the warm season.

The Heidke skill score performance of the MiRS and MSPPS precipitation algorithms is shown in Fig. 6(e). Both precipitation algorithms have shown similar capabilities to correctly estimate precipitating conditions. This is a similar observation obtained when analyzing the performance of the MiRS and MSPPS precipitation algorithms over the CONUS region. On the other hand, in Fig. 6(f), it is clear that the MSPPS precipitation algorithm has larger rmse values than those seen for the MiRS precipitation algorithm, particularly over the warm season. The differences in the rmse values found between the MSPPS and MiRS algorithms are consistently on the order of 5.0 mm/day or more. The large rmse values associated with the MSPPS algorithm are a consistent result that has also been found in the comparisons carried out over the CONUS region.

3) Assessment Over the Australian Region: The third region under analysis is the Australian region. As in the other region cases, the results related to this region are shown in Fig. 7 in the form of time series of statistics. Over Australia, the MiRS, MSPPS, MWCOMB, and 3B40RT precipitation algorithms are the satellite-based microwave algorithms that have been validated on a daily basis for more than one year.

The first parameter to analyze in this validation/comparison is the bias. As observed in Fig. 7(a), this parameter shows values consistently closer to 0 mm/day for all precipitation algorithms, particularly from April to October 2009 (winter season). With respect to the correlation values reported in Fig. 7(b), all of the microwave-based precipitation algorithms show a low correlation performance from April 2009 to October 2009 and from April 2010 to June 2010. This interval corresponds to the same time when the bias has consistently reported the lowest bias values for all precipitation algorithms. From the results shown in Fig. 7(b), the MiRS precipitation algorithm reports a comparable correlation performance than the one observed for the 3B40RT and MWCOMB algorithms. The low correlation values observed for the MiRS and MSPPS precipitation algorithms around the beginning of 2009 are associated with the fact that, for several days, no rainfall was produced by the precipitation algorithms during this period of time.

In Fig. 7(c), the probability of detection performance is reported. In this figure, a clear seasonal dependence is observed in all precipitation algorithms. For instance, the lowest values of probability of detection are about 0.20 near the peak of the winter season (about July 2009), while values near 0.50 are reported close to the peak of the warm season (January 2009 and 2010). In the case of the false alarm rate performance shown in Fig. 7(d), small and steady values have been observed during the April 2009 to September 2009 period (winter season), while large and variable values are found during the October 2009 to March 2010 period (warm season). The seasonal dependence observed in the performance of the false alarm rate and probability of detection is in agreement with respect to the results found over the CONUS and South American regions. Fig. 7(d) shows that the magnitude of the false alarm rate values is, in most of the cases, lower than 0.1, with the MiRS precipitation algorithm generally showing similar results to the 3B40RT and MWCOMB algorithms.

The Heidke skill score results reported in Fig. 7(e) shows that the precipitation algorithms have similar performance characteristics, including the seasonal dependence. The major differences in the Heidke skill score are observed at the beginning of 2009, where the MiRS and MSPPS precipitation algorithms show low Heidke skill score values. This result is related to the lack of rainfall produced by these algorithms during this time period. On the other hand, Fig. 7(f) shows that the larger rmse values occur during the October 2009 to March 2010 period (warm season), while the lowest rmse values occur during the April to September 2009 period (winter season). The MiRS precipitation has consistently shown comparable rmse values with respect to the 3B40RT and MWCOMB precipitation estimates. The magnitude of the rmse values of the MiRS precipitation estimate that has been observed over Australia is in agreement with the rmse values observed over the CONUS and South American regions.

In general, after analyzing the performance of the MiRS precipitation estimation algorithm over three regions located at different latitudes and over different seasons against the rain gauge and rain radar observations, the MiRS precipitation algorithm has shown similar capabilities to other satellite-based microwave precipitation estimation algorithms, including the MWCOMB, 3B40RT, and MSPPS precipitation algorithms. As observed in other satellite-based microwave precipitation algorithms, the MiRS precipitation algorithm has shown a better performance in detecting rainy conditions during warm seasons than during winter seasons. This result is expected due to the difficulties of the MiRS algorithm to detect light precipitation that are more typical during the winter seasons, particularly over the land surfaces, where a small brightness temperature contrast is observed at the microwave emission channels. The low false alarm rate and relatively low detection rate of the MiRS precipitation algorithm in the warm season are a known and expected feature. In part, this feature is explained by the low resolution (about 50 km) of the MiRS precipitation estimates, which reduces the detection of high precipitation that are particularly observed over precipitation systems with small features, like thunderstorms, during the warm season. The MiRS precipitation has also shown one of the lowest bias values and lowest magnitudes of rmse values, as well as high correlation values, particularly over the warm season.

In the comparisons presented throughout Section IV-C, the impact of the different number of sensors used to compute the daily precipitation composite estimates must be accounted for. In this respect, the better general performance shown by the 3B40RT or MWCOMB algorithm with respect to the MiRS and MSPPS algorithms is partially due to the better spatial and temporal coverage associated with those algorithms, which process more satellite sensors. This condition could possibly explain the large rmse values reported by the MSPPS algorithm, which uses only two sensors to determine the daily precipitation composite estimates.

D. Assessment Using the Monthly MSPPS Precipitation Composite Estimate

Although an extensive comparison between the performance of the MiRS and MSPPS precipitation estimates has been presented in Section IV-C, in this section, a further assessment of the MiRS precipitation has been carried out using the MSPPS global monthly precipitation composite product. This type of comparison is performed on a regular basis in order to observe seasonal and/or climatic features. In addition, by observing the monthly precipitation composite, a more clear detection of some characteristics of the MiRS precipitation estimate is allowed due to the reduction of the high temporal variability of the precipitation. The MiRS is expected to gradually replace the MSPPS system in the next years. Therefore, it is important to compare the performance of both systems. Currently, the MSPPS is being applied operational to several satellites, including NOAA-15, NOAA-16, NOAA-17, NOAA-18, NOAA-19, and Metop-A.

Fig. 8 shows the comparison between the MiRS and MSPPS global monthly rainfall rate composite corresponding to September and October 2009. These results were generated based on observations from the AMSU and MHS sensors onboard the NOAA-18 and Metop-A satellites. The composites shown in Fig. 8 are generated at 1° resolution. The original resolution of the MiRS rainfall rate is that of the AMSU sensor ($\sim$50 km), while the original resolution of the MSPPS rainfall

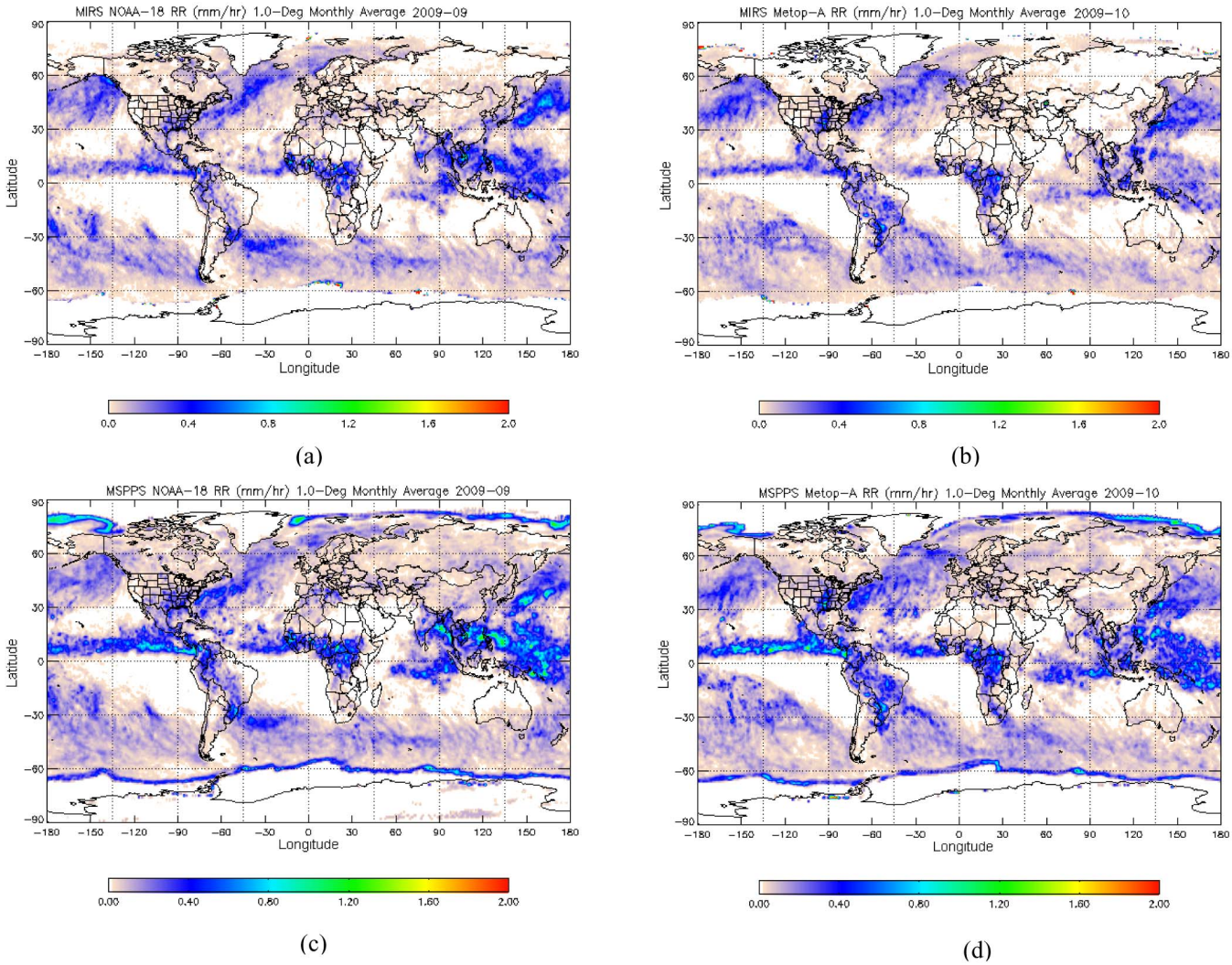

Fig. 8. 1° resolution global monthly rainfall rate composite products given in millimeters per hour corresponding to (a) MiRS NOAA-18 for September 2009, (b) MiRS Metop-A for October 2009, (c) MSPPS NOAA-18 for September 2009, and (d) MSPPS Metop-A for October 2009.

rate products is that of the MHS sensor (∼15 km). In Fig. 8, it is observed that, in general, the MiRS and MSSPS precipitation algorithms retrieve precipitation over similar regions, but the MSPPS algorithm tends to estimate higher rainfall rate values than the MiRS precipitation algorithm, especially over the tropics. Information about the positive bias of the MSPPS precipitation has been reported previously in [4], when compared against the rain gauge analysis on the monthly time scale.

In Fig. 8, persistent false alarms at the sea-ice edges are clearly observed in the MSPPS precipitation. This is due to the mixed signal in the brightness temperatures for which the MSPPS precipitation algorithm is not trained. On the other hand, the MiRS precipitation shows a significant reduction in the false alarms at the sea-ice edges. This important property of the MiRS precipitation is associated with the capability of the MiRS to distinguish properly between land, ocean, sea-ice, and snow surfaces. Since the MiRS directly incorporates the emissivity spectrum as part of the retrieved state vector, it is able to explicitly account for the mixed surface signal (instead of using the atmospheric parameters). This property makes the MiRS precipitation a more efficient and reliable product over the sea-ice edges as compared to the MSPPS precipitation.

E. Assessment Using Frequency Distribution Histograms of the TRMM-2A12 and WRF Hydrometeors

In this section, additional information about the characteristics of the hydrometeors retrieved by the MiRS is presented. Figs. 9–11 show a comparison of the frequency distribution histograms of the MiRS CLWP, RWP, IWP, and rainfall rate versus the TRMM-2A12 version 6.0 and WRF model Version 3.1 hydrometeors derived over tropical ocean and land surfaces. The MiRS and TRMM-2A12 results are based on one year of temporal and spatial collocations performed between the NOAA-18 AMSU/MHS and the TMI. The WRF results are based on separate simulations performed over the tropics using the Goddard Cumulus Ensemble [38] as the cloud resolving model. The WRF and TRMM-2A12 hydrometeors were spatially averaged to the resolution of the MiRS hydrometeor products (i.e., approximately 50 km). Results related to the ability of the WRF to produce hydrometeors are reported in

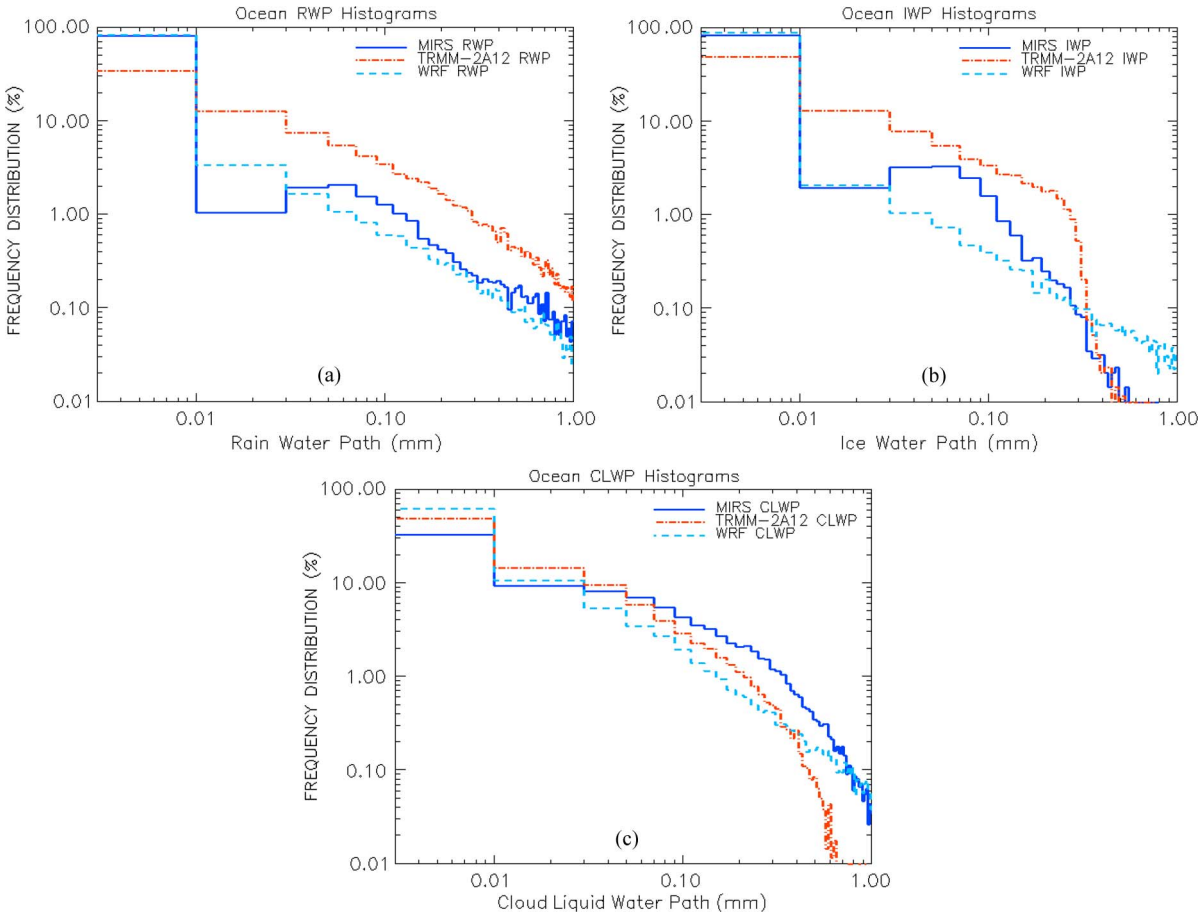

Fig. 9. Frequency distribution histograms of (a) RWP, (b) IWP, and (c) CLWP greater than zero over the ocean, derived from the MiRS, TRMM-2A12, and WRF model.

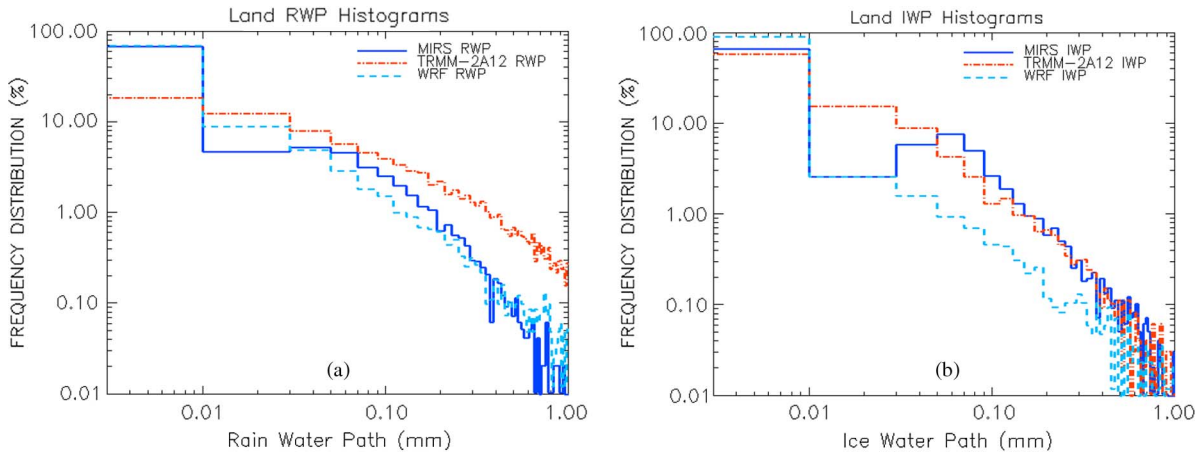

Fig. 10. Frequency distribution histograms of (a) RWP and (b) IWP greater than zero over the land, derived from the MiRS, TRMM-2A12, and WRF model.

[39], while information about the characteristics of the TRMM-2A12 hydrometeors can be found in [6], [40], and [41].

Figs. 9 and 10 show that the MiRS RWP has a similar frequency distribution with the WRF RWP over the ocean and land. For both surface types, the MiRS RWP shows a decrease in frequency distribution for RWP values approximately varying between 0.01 and 0.03 mm. Compared to the MiRS and WRF RWP histograms, the TRMM-2A12 RWP shows lower frequency distribution values for RWP less than 0.01 mm but consistently larger frequency distribution values for RWP greater than 0.01 mm over the ocean and land. In the case of the IWP over the ocean, the MiRS IWP shows a good agreement with respect to the WRF IWP for IWP values that are less than 0.03 mm. Over land, the MiRS IWP has a better agreement with respect to the TRMM-2A12 IWP for IWP values above 0.03 mm. As observed with the MiRS RWP, the MiRS IWP has a decrease in the frequency distribution for IWP values varying between 0.01 and 0.03 mm. Since the MiRS simultaneously

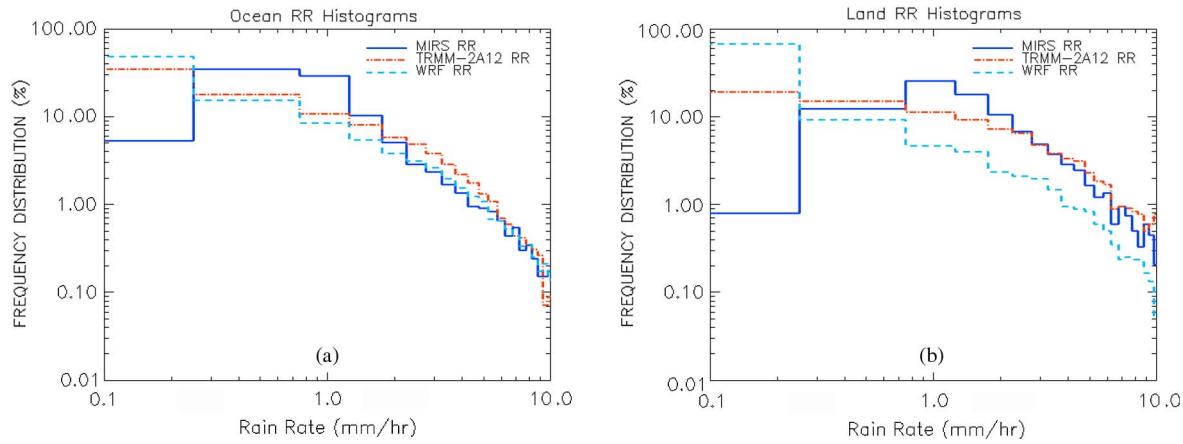

Fig. 11. Frequency distribution histograms of rainfall rate (RR) greater than zero derived from the MiRS, TRMM-2A12, and WRF model over the (a) ocean and (b) land.

retrieves a set of atmospheric and surface parameters, it is possible that, in situations where the precipitation signal is weak (e.g., light rain), the MiRS is able to find a physical solution solely by varying the geophysical state vector in the first attempt of the 1-DVAR (including the absorption effects of CLW) without accounting for the absorption and scattering effects associated with larger hydrometeors (rain and ice water) that are retrieved in the second attempt of the MiRS. This could explain the decrease in the frequency distribution of the MiRS RWP and IWP for the 0.01–0.03-mm range that is associated with weaker precipitation signals. With respect to the CLWP, Fig. 9(c) shows that the MiRS CLWP tends to have lower frequency distribution values than WRF and TRMM-2A12 for CLWP values below 0.03 mm but consistently larger values for CLWP values greater than 0.05 mm.

Fig. 11 shows the frequency distribution of the MiRS, WRF, and TRMM-2A12 rainfall rates over the ocean and land for cases where the rainfall rate is greater than 0 mm/h. In Fig. 11(a), it is observed that the frequency distribution of the MiRS rainfall rate over the ocean is significantly lower than both TRMM and WRF for rain rate values less than 0.25 mm/h. Based on the values of the regression coefficients reported in (4) that are used for the estimation of the MiRS rainfall rate over the ocean, it is found that this performance is related to the low frequency distribution values of RWP and IWP retrieved by the MiRS mainly over the 0.01–0.03-mm range, as can be verified from Fig. 9(a) and (b). As shown in Fig. 11(b), over land, a similar situation is observed by noticing that the MiRS rainfall rate frequency distribution decreases for rain rate values below 0.75 mm/h. In this case, the effect of the MiRS retrieving less rain and ice water between 0.01 and 0.03 mm is extended to 0.75 mm/h due to the large RWP and IWP regression coefficients used for the estimation of the precipitation over land, as can be verified from (5). From the results shown in Fig. 11(a), it is observed that, over the ocean, the MiRS estimates larger amounts of rainfall rate than WRF and TRMM-2A12 over the 0.25–1.25-mm/h range. Over land, a similar performance is observed but for rainfall rate values between 0.75 and 2.25 mm/h, as shown in Fig. 11(b). Over the ocean, it is found that the MiRS rainfall rate shows a better agreement with respect to the WRF and TRMM-2A12 rainfall rate frequency distribution for rainfall rate values above 1.25 mm/h. However, the TRMM-2A12 rainfall rate shows consistently large frequencies than the MiRS and WRF for rainfall rate values between 1.75 and 6.75 mm/h. Over land, the rainfall rate distribution of the MiRS agrees much better with the TRMM-2A12 distribution for rainfall rates greater than 2.25 mm/h.

The results presented here show the impact of the quality of the hydrometeors retrieved by the MiRS in the estimation of the rainfall rate. An improvement in the retrieval of the RWP and IWP, particularly in the 0.01–0.03-mm range, is needed to improve the estimation of rainfall rates below 1.0 mm/h over the ocean and below 2.0 mm/h over land. The results also show that, over the ocean, a better agreement over a large range of rainfall rates is found between the MiRS rainfall rate and both TRMM-2A12 and WRF rainfall rates. This result is related to the better capability of the MiRS to retrieve hydrometeors over the ocean (low and nearly stable surface emissivity) than over land (high and variable surface emissivity) from microwave observations.

V. Conclusion

This paper has presented the development and assessment of a rainfall rate postprocessing relationship that uses hydrometeors, including, CLW, rain water, and ice water derived by the MiRS, to retrieve the surface precipitation rates in millimeters per hour. Since the relationship relies on the hydrometeor products retrieved by the physically based MiRS and not on the sensor-dependent parameters, it is generic to all capable microwave sensors to which the MiRS is being applied.

Through the development of the MiRS precipitation technique and the extensive assessment efforts carried out using rain gauge, ground-based radar observations, and satellite-based microwave precipitation estimates as precipitation references, the capabilities of the MiRS precipitation technique to estimate precipitation over land and ocean surfaces have been presented and evaluated. In general, it has been observed that the MiRS precipitation technique is able to estimate precipitation with similar characteristics to other satellite-based microwave precipitation estimation algorithms. This is noteworthy considering that the MiRS precipitation estimation technique is only one component of the MiRS, which is not merely designed

to retrieve the rainfall rate but to simultaneously retrieve a set of surface and atmospheric parameters, including the emissivity spectrum, skin temperature, water vapor, temperature, and hydrometeor profiles; all of which are consistently retrieved from microwave measurements.

The MiRS precipitation estimation technique has been developed to be applied on current and future sensors and to facilitate its transition from research to operations. Currently, this technique has been successfully applied operationally to several satellite-based microwave sensors, including NOAA-18, NOAA-19, Metop-A AMSU/MHS, and DMSP-F16 and DMSP-F18 SSMI/S.

From the comparisons against the rain gauges and rain radar observations over land, it was observed that the performance of the MiRS precipitation is seasonally dependent. In general, the capabilities of the MiRS precipitation technique to detect rainy conditions are better during the warm seasons than during the winter seasons. This result is related to the difficulties associated to the MiRS technique to detect light precipitation that is more common during the winter than in the summer season. Over land, the high and variable surface emissivity makes the microwave emissions as a weak source of information, particularly affecting the estimation of light precipitation. This characteristic is not a property of the MiRS precipitation technique but is a property that has been generally observed in satellite-based microwave precipitation algorithms and that has been consistently reported in previous work [13], [18].

It is important to mention that the reported errors in the satellite precipitation estimates could be larger than their true values because the observation errors in the reference data contribute to the total error, i.e., uncertainties in the reference data themselves may contribute to the decreases in the estimates of the algorithm performance. For example, the actual rmse errors of the precipitation estimates could be slightly smaller, while the correlations could be somewhat higher. In the case of the categorical statistics (probability of detection, false alarm rate, and Heidke skill score), unless the reference data had systematic tendencies to over- or under-detect rainfall, results would probably not change significantly since these metrics are less sensitive to the magnitude of the rainfall.

Finally, efforts are being taken not only to improve the capabilities of the MiRS precipitation algorithm to detect rainy conditions but also to reduce the seasonal dependence of the algorithm. For this purpose, two major efforts are being carried out. One involves the computation of new regression coefficients for different seasons, regions, and cloud types using a similar approach to that used in deriving the coefficients reported in (4) and (5), which would allow the MiRS precipitation estimation technique to respond more dynamically and efficiently to different atmospheric conditions. The other strategy involves the development of a hydrometeor background covariance matrix for the MiRS, stratified by precipitation type, latitude, and season, which could improve the retrieving of hydrometeors over different season and regions. The necessity of an improvement in quality of the MiRS hydrometeors, particularly in the 0.01–0.03-mm range, has been identified, and it is expected to improve the estimation of the rainfall rate below 1.0 mm/h over the ocean and below 2.0 mm/h over land. With these efforts, an enhancement in the performance of the MiRS precipitation technique over different seasons and latitudes is expected.

ACKNOWLEDGMENT

The authors would like to thank J. Janowiak from the University of Maryland, D. Vila from the Instituto Nacional de Pesquisas Espaciais, and E. Ebert from the Australian Bureau of Meteorology Research Centre for processing the MiRS rainfall rates within the IPWG and for providing an independent validation of the MiRS precipitation algorithm. In addition, the authors thank the anonymous reviewers for their helpful comments which improved this paper.

REFERENCES

[1] C. Kummerow, J. Simpson, O. Thiele, W. Barnes, A. T. C. Chang, E. Stocker, R. F. Adler, A. Hou, R. Kakar, F. Wentz, P. Ashcroft, T. Kozu, Y. Hong, K. Okamoto, T. Iguchi, H. Kuroiwa, E. Im, Z. Haddad, G. Huffman, B. Ferrier, W. S. Olson, E. Zipser, E. A. Smith, T. T. Wilheit, G. North, T. Krishnamurti, and K. Nakamura, "The status of the Tropical Rainfall Measuring Mission (TRMM) after two years in orbit," *J. Appl. Meteorol.*, vol. 39, no. 12, pp. 1965–1982, Dec. 2000.

[2] P. A. Arkin and B. N. Meisner, "The relationship between large-scale convective rainfall and cold cloud over the Western Hemisphere during 1982–84," *Monthly Weather Rev.*, vol. 115, no. 1, pp. 51–74, Jan. 1987.

[3] T. T. Wilheit, R. Adler, S. Avery, E. Barrett, P. Bauer, W. Berg, A. Chang, J. Ferriday, N. Grody, S. Goodman, C. Kidd, D. Kniveton, C. Kummerow, A. Mugnai, W. Olson, G. Petty, A. Shibata, E. Smith, and R. Spence, "Algorithms for the retrieval of rainfall from passive microwave measurements," *Remote Sens. Rev.*, vol. 11, no. 1–4, pp. 163–194, Oct. 2004.

[4] R. R. Ferraro, F. Weng, N. C. Grody, L. Zhao, H. Meng, C. Kongoli, P. Pellegrino, S. Qiu, and C. Dean, "NOAA operational hydrological products derived from the Advanced Microwave Sounding Unit," *IEEE Trans. Geosci. Remote Sens.*, vol. 43, no. 5, pp. 1036–1049, May 2005. doi:10.1109/TGRS.2004.843249.

[5] G. W. Petty, "Physical retrievals of over-ocean rain rate from multichannel microwave imagery. Part II: Algorithm implementation," *Meteorol. Atmos. Phys.*, vol. 54, no. 1–4, pp. 101–121, Mar. 1994.

[6] C. D. Kummerow, Y. Hong, W. S. Olson, S. Yang, R. F. Adler, J. McCollum, R. Ferraro, G. Petty, D. B. Shin, and T. T. Wilheit, "The evolution of the Goddard Profiling Algorithm (GPROF) for rainfall estimation from passive microwave sensors," *J. Appl. Meteorol.*, vol. 40, no. 11, pp. 1801–1820, Nov. 2001.

[7] C. Surussavadee and D. H. Staelin, "Satellite retrievals of Arctic and Equatorial rain and snowfall rates using millimeter wavelengths," *IEEE Trans. Geosci. Remote Sens.*, vol. 47, no. 11, pp. 3697–3707, Nov. 2009.

[8] R. F. Adler, A. J. Negri, P. R. Keehn, and I. M. Hakkarinen, "Estimation of monthly rainfall over Japan and surrounding waters from a combination of low-orbit microwave and geosynchronous IR data," *J. Appl. Meteorol.*, vol. 32, no. 2, pp. 335–356, Feb. 1993.

[9] R. J. Joyce, J. E. Janowiak, P. A. Arkin, and P. Xie, "CMORPH: A method that produces global precipitation estimates from passive microwave and infrared data at high spatial and temporal resolution," *J. Hydrometeorol.*, vol. 5, no. 3, pp. 487–503, Jun. 2004.

[10] F. J. Turk and S. D. Miller, "Toward improved characterization of remotely sensed precipitation regimes with MODIS/AMSR-E blended data techniques," *IEEE Trans. Geosci. Remote Sens.*, vol. 43, no. 5, pp. 1059–1069, May 2005.

[11] G. J. Huffman, R. F. Adler, D. T. Bolvin, G. Gu, E. J. Nelkin, K. P. Bowman, Y. Hong, E. F. Stocker, and D. B. Wolff, "The TRMM Multisatellite Precipitation Analysis (TMPA): Quasi-global, multiyear, combined-sensor precipitation estimates at fine scales," *J. Hydrometeorol.*, vol. 8, no. 1, pp. 38–55, Feb. 2007.

[12] T. Ushio, K. Sasashige, T. Kubota, S. Shige, K. Okamoto, K. Aonashi, T. Inoue, N. Takahashi, T. Iguchi, M. Kachi, R. Oki, T. Morimoto, and Z. Kawasaki, "A Kalman filter approach to the Global Satellite Mapping of Precipitation (GSMaP) from combined passive microwave and infrared radiometric data," *J. Meteorol. Soc. Japan*, vol. 87A, pp. 137–151, Aug. 2009.

[13] E. E. Ebert, M. J. Manton, P. A. Arkin, R. J. Allam, C. E. Holpin, and A. Gruber, "Results from the GPCP algorithm intercomparison programme," *Bull. Amer. Meteorol. Soc.*, vol. 77, no. 12, pp. 2875–2887, Dec. 1996.
[14] R. F. Adler, G. J. Huffman, A. Chang, R. Ferraro, P. Xie, J. Janowiak, B. Rudolf, U. Schneider, S. Curtis, D. Bolvin, A. Gruber, J. Susskind, P. Arkin, and E. Nelkin, "The version-2 Global Precipitation Climatology Project (GPCP) monthly precipitation analysis (1979–present)," *J. Hydrometeorol.*, vol. 4, no. 6, pp. 1147–1167, Dec. 2003.
[15] E. C. Barrett, R. F. Adler, K. Arpe, P. Bauer, W. Berg, A. Chang, R. Ferraro, J. Ferriday, S. Goodman, Y. Hong, J. Janowiak, C. Kidd, D. Kniveton, M. Morrissey, W. Olson, G. Petty, B. Rudolf, A. Shibata, E. Smith, and R. Spencer, "The first WetNet Precipitation Intercomparison Project (PIP-1): Interpretation of results," *Remote Sens. Rev.*, vol. 11, no. 1–4, pp. 303–373, Oct. 1994.
[16] E. A. Smith, J. E. Lamm, R. Adler, J. Alishouse, K. Aonashi, E. Barrett, P. Bauer, W. Berg, A. Chang, R. Ferraro, J. Ferriday, S. Goodman, N. Grody, C. Kidd, D. Kniveton, C. Kummerow, G. Liu, F. Marzano, A. Mugnai, W. Olson, G. Petty, A. Shibata, R. Spencer, F. Wentz, T. Wilheit, and E. Zipser, "Results of WetNet PIP-2 Project," *J. Atmos. Sci.*, vol. 55, no. 9, pp. 1483–1536, May 1998.
[17] R. F. Adler, C. Kidd, G. Petty, M. Morissey, and H. M. Goodman, "Intercomparison of global precipitation products: The Third Precipitation Intercomparison Project (PIP-3)," *Bull. Amer. Meteorol. Soc.*, vol. 82, no. 7, pp. 1377–1396, Jul. 2001.
[18] E. E. Ebert, J. E. Janowiak, and C. Kidd, "Comparison of near-real-time precipitation estimates from satellite observations and numerical models," *Bull. Amer. Meteorol. Soc.*, vol. 88, no. 1, pp. 47–64, Jan. 2007.
[19] F. J. Turk, P. Arkin, E. E. Ebert, and M. R. P. Sapiano, "Evaluating high-resolution precipitation products," *Bull. Amer. Meteorol. Soc.*, vol. 89, no. 12, pp. 1911–1916, Dec. 2008.
[20] B. Lambrigtsen, A. Tanner, T. Gaier, P. Kangaslahti, and S. Brown, "Developing a GeoSTAR science mission," in *Proc. IEEE Geosci. Remote Sens. Symp.*, 2007, pp. 5232–5236.
[21] G. M. Flaming, "Requirements for global precipitation measurement," in *Proc. IEEE Geosci. Remote Sens. Symp.*, 2002, vol. 1, pp. 269–271.
[22] D. A. Newell, D. Figgins, T. Ta, and B. Berdanier, "GPM microwave imager instrument design and predicted performance," in *Proc. IEEE Geosci. Remote Sens. Symp.*, 2007, pp. 4426–4428.
[23] S.-A. Boukabara, F. Weng, and Q. Liu, "Passive microwave remote sensing of extreme weather events using NOAA-18 AMSUA and MHS," *IEEE Trans. Geosci. Remote Sens.*, vol. 45, no. 7, pp. 2228–2246, Jul. 2007.
[24] S.-A. Boukabara, K. Garrett, W. Chen, F. Iturbide-Sanchez, C. Grassotti, C. Kongoli, R. Chen, Q. Liu, B. Yan, F. Weng, R. Ferraro, T. Kleespies, and H. Meng, "MiRS: An all-weather 1DVAR satellite data assimilation & retrieval system," *IEEE Trans. Geosci. Remote Sens.*, to be published.
[25] C. D. Rodgers, *Inverse Methods for Atmospheric Sounding: Theory and Practice*. Singapore: World Scientific, 2000.
[26] F. Weng, Y. Han, P. Van Delst, Q. Liu, T. Kleespies, B. Yan, and J. Le Marshall, "JCSDA Community Radiative Transfer Model (CRTM)," in *Proc. 14th TOVS Conf.*, Beijing, China, 2005, pp. 217–222.
[27] Y. Han, P. Van Delst, Q. Liu, F. Weng, B. Yan, R. Treadon, and J. Derber, "Community Radiative Transfer Model (CRTM)," Dept. Commerce, Washington, DC, NOAA Technical Report 122, 2006, version 1.
[28] F. Weng, L. Zhao, G. Poe, R. Ferraro, X. Li, and N. Grody, "Advanced Microwave Sounding Unit cloud and precipitation algorithms," *Radio Sci.*, vol. 38, no. 4, p. 8068, Jun. 2003. doi:10.1029/2002RS002679.
[29] G. A. Grell, J. Dudhia, and D. R. Stauffer, "A description of the fifth-generation Penn State/NCAR Mesoscale Model (MM5)," Nat. Center Atmos. Res., Boulder, CO, NCAR Tech. Note NCAR/TN-398, Jun. 1995.
[30] S. Kida, S. Shiqe, T. Manabe, T. S. L'Ecuyer, and G. Liu, "Validation of rain/no-rain threshold value of cloud liquid water for microwave precipitation retrieval algorithm using CloudSat precipitation product," in *Proc. SPIE*, 2008, vol. 7152, pp. 715 209-1–715 209-8.
[31] B. A. Colle, C. F. Mass, and K. J. Westrick, "MM5 precipitation verification over the Pacific Northwest during the 1997–99 cool seasons," *Weather Forecasting*, vol. 15, no. 6, pp. 730–744, Dec. 2000.
[32] B. A. Colle, J. B. Olson, and J. S. Tongue, "Multiseason verification of the MM5. Part II: Evaluation of high-resolution precipitation forecasts over the Northeastern United States," *Weather Forecasting*, vol. 18, no. 3, pp. 458–480, Jun. 2003.
[33] W. Wang and N. L. Seaman, "A comparison study of convective parameterization schemes in a mesoscale model," *Monthly Weather Rev.*, vol. 125, no. 2, pp. 252–278, Feb. 1997.
[34] G. Goodrum, K. B. Kidwell, and W. Winston, *NOAA KLM User's Guide*. Silver Spring, MD: Nat. Ocean. Atmos. Admin., 1999.
[35] D. B. Kunkee, G. A. Poe, D. J. Boucher, S. D. Swadley, Y. Hong, J. E. Wessel, and E. A. Uliana, "Design and evaluation of the first Special Sensor Microwave Imager/Sounder," *IEEE Trans. Geosci. Remote Sens.*, vol. 46, no. 4, pp. 863–883, Apr. 2008.
[36] Y. Lin and K. E. Mitchell, "The NCEP stage II/IV hourly precipitation analyses: Development and applications," presented at the Proc. 19th Conf. Hydrol., Amer. Meteorol. Soc., San Diego, CA, 2005, Paper 1.2.
[37] G. J. Huffman, "Estimates of root-mean-square random error for finite samples of estimated precipitation," *J. Appl. Meteorol.*, vol. 36, no. 9, pp. 1191–1201, Sep. 1997.
[38] W.-K. Tao, J. Simpson, D. Baker, S. Braun, M.-D. Chou, B. Ferrier, D. Johnson, A. Khain, S. Lang, B. Lynn, C.-L. Shie, D. Starr, C.-H. Sui, Y. Wang, and P. Wetzel, "Microphysics, radiation and surface processes in the Goddard Cumulus Ensemble (GCE) model," *Meteorol. Atmos. Phys.*, vol. 82, no. 1–4, pp. 97–137, Jan. 2003.
[39] J. J. Shi, W.-K. Tao, T. Matsui, R. Cifelli, A. Hou, S. Lang, A. Tokay, N.-Y. Wang, C. Peters-Lidard, G. Skofronick-Jackson, S. Rutledge, and W. Petersen, "WRF simulations of the 20–22 January 2007 snow events over Eastern Canada: Comparison with *in situ* and satellite observations," *J. Appl. Meteorol. Climatol.*, vol. 49, no. 11, pp. 2246–2266, Nov. 2010.
[40] W. S. Olson, C. D. Kummerow, S. Yang, G. W. Petty, W.-K. Tao, T. L. Bell, S. A. Braun, Y. Wang, S. E. Lang, D. E. Johnson, and C. Chiu, "Precipitation and latent heating distributions from satellite passive microwave radiometry. Part I: Improved Method and Uncertainties," *J. Appl. Meteorol. Climatol.*, vol. 45, no. 5, pp. 702–720, May 2006.
[41] S. T. Fiorino and E. A. Smith, "Critical assessment of microphysical assumptions within TRMM radiometer rain profile algorithm using satellite, aircraft, and surface data sets from KWAJEX," *J. Appl. Meteorol. Climatol.*, vol. 45, no. 5, pp. 754–786, May 2006.

Flavio Iturbide-Sanchez (S'03–M'07) received the B.S.E.E degree in electronics engineering from the Autonomous Metropolitan University, Mexico City, Mexico, in 1999, the M.S.E.E. degree in electrical engineering from the Advanced Studies and Research Center, National Polytechnic Institute, Mexico City, in 2001, and the Ph.D. degree from the University of Massachusetts, Amherst, in 2007, where he was advised by Prof. S. C. Reising and was supported by the National Science Foundation.

His Ph.D. research focused on the miniaturization, development, calibration, and performance assessment of low-cost and power-efficient microwave radiometers for remote sensing applications. From 2001 to 2005, he was a Research Assistant with the Microwave Remote Sensing Laboratory, University of Massachusetts, where he performed research on the design, development, and characterization of highly integrated multichip modules and microwave circuits for low-noise, low-power consumption, high-gain, and high-stability microwave radiometers. From 2005 to 2007, he was with the Microwave Systems Laboratory, Colorado State University, Fort Collins, focusing on design, testing, deployment, and data analysis of the low-cost and power-efficient compact microwave radiometer for humidity profiling. Since 2008, he has been with the I.M. Systems Group, Inc., National Oceanic and Atmospheric Administration/National Environmental Satellite, Data, and Information Service/Center for Satellite Applications and Research, Camp Springs, MD. His research interests include communication systems; microwave radiometry; microwave/millimeter-wave IC design and packaging; RF integrated circuits; system-on-a-chip; active antennas; modeling, analysis, design, and measurement of microwave and millimeter-wave circuits and systems; and atmospheric remote sensing, including retrieval algorithm development.

Dr. Iturbide-Sanchez won a First-Place Poster Award at the 11th Specialist Meeting on Microwave Radiometry and Remote Sensing Applications (MicroRad 2010) in Washington, DC. While a Ph.D. student, he was a finalist in two IEEE Student Paper Competitions: one at the International Geoscience and Remote Sensing Symposium in Anchorage, AK, in September 2004 and one at the International Microwave Symposium in San Francisco, CA, in June 2006. He was also awarded the Mexican National Council for Science and Technology (CONACYT) Graduate Fellowship from 1999 to 2004.

Sid-Ahmed Boukabara received the Engineer degree in signal processing from the National School of Civil Aviation (ENAC), Toulouse, France, in 1994, the M.S. degree in signal processing from the Institut National Polytechnique de Toulouse, Toulouse, in 1994, and the Ph.D. degree in remote sensing from the Denis Diderot University, Paris, France, in 1997.

He was then involved in the calibration/validation of the European Space Agency's ERS-2 microwave radiometer, and he has worked on the synergistic use of active and passive microwave measurements. He then joined AER Inc., Cambridge, MA, as a Staff Scientist and worked on the design, implementation, and validation of the NPOESS/CMIS physical retrieval algorithm on the NASA SeaWinds/QuikSCAT wind vector rain flag and on the development of the atmospheric absorption model MonoRTM dedicated to microwave and laser applications. In 2005, he joined the National Oceanic and Atmospheric Administration/National Environmental Satellite, Data, and Information Service, Camp Springs, MD, where he currently leads an effort to develop the capability of assimilating passive microwave measurements in all-weather conditions using a combination of variational technique algorithm and the community radiative transfer model. Since 2009, he has also been serving as the Deputy Director of the U.S. Joint Center for Satellite Data Assimilation. His principal areas of interest include radiative transfer modeling, spectroscopy, algorithm development, and satellite data assimilation.

Ruiyue Chen received the B.S. and M.S. degrees in electrical engineering from the Nanjing University of Aeronautics and Astronautics, Nanjing, China, in 1997 and 2000, respectively, the M.S. degree in atmospheric sciences from Texas A&M University, College Station, in 2003, and the Ph.D. degree in atmospheric sciences from the University of Maryland, College Park, in 2010.

In 2007, he joined the I.M. Systems Group, Rockville, MD, in support of satellite remote sensing and sensor calibration for the National Environmental Satellite Data and Information Service, National Oceanic Atmospheric Administration. His principal areas of interest include microwave remote sensing and satellite sensor calibration.

Kevin Garrett received the M.S. degree in atmospheric sciences from Texas A&M University, College Station, in 2007.

He then joined the I.M. Systems Group, National Oceanic and Atmospheric Administration (NOAA)/National Environmental Satellite, Data, and Information Service, Camp Springs, MD, as a Physical Scientist. He is currently leading the effort of integrating NOAA's Microwave Integrated Retrieval System within the NPOESS Data Exploitation operational environment. His primary effort is focused on the development of passive microwave remote sensing retrieval algorithms.

Christopher Grassotti received the B.S. degree in earth and space science from the State University of New York, Stony Brook, the M.S. degree in atmospheric science from the University of Wisconsin, Madison, and the M.S. degree in viticulture and enology from the Ecole Nationale Superieure Agronomique (now SupAgro), Montpellier, France.

He was with the Atmospheric and Environmental Research, Inc., Lexington, MA, and Environment Canada, Montreal, QC, Canada. He is currently with the I.M. Systems Group, Camp Springs, MD, as a Contractor for the National Oceanic and Atmospheric Administration/National Environmental Satellite, Data, and Information Service/Satellite Applications and Research, focusing on development and improvements in the Microwave Integrated Retrieval System.

Wanchun Chen received the B.S degree in atmospheric science from the Beijing Institute of Meteorology, Beijing, China, in 1994 and the M.S. degree in meteorology from the University of Maryland, College Park, in 2000.

He is with Dell Inc., National Oceanic and Atmospheric Administration/National Environmental Satellite, Data, and Information Service/Center for Satellite Applications and Research, Camp Springs, MD, where he is working as a Systems and Web Developer in the Microwave Integrated Retrieval System.

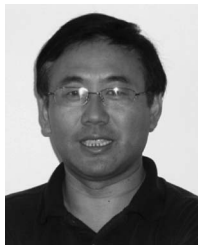

Fuzhong Weng received the Ph.D. degree from the Department of Atmospheric Science, Colorado State University, Fort Collins, in 1992.

He is the Chief of the Satellite Calibration and Data Assimilation Branch, National Oceanic and Atmospheric Administration (NOAA)/National Environmental Satellite, Data, and Information Service/Center for Satellite Applications and Research, Camp Springs, MD. In the past years, he led the developments of the NOAA operational satellite microwave products and algorithms from the Special Sensor Microwave Imager and Advanced Microwave Sounding Unit. He is the Sensor Science Chair of the NPP/JPSS program. He is the Science Lead in developing the community radiative transfer model that has been successfully used in several operational data assimilation systems in the U.S. He also directly contributed in developments of microwave land, snow, and sea-ice emissivity models which have significantly improved the uses of satellite sounding data in NWP models and have impacted the high-latitude weather forecasts. He is currently developing new innovative techniques to advance uses of satellite measurements under cloudy and precipitation areas in NWP models. He has published over 80 papers in international peer-reviewed journals.

Dr. Weng was the first winner of the 2000 NOAA David Johnson Award for his outstanding contributions to the satellite microwave remote sensing fields and the utilization of satellite data in the NWP models. He also received the 2002 SPIE Scientific Achievement Award for Excellence in Developing Operational Satellite Microwave Products and Algorithms. He was awarded in 2004 by the U.S. Department of Commerce with bronze medal for his developments of operational microwave products to improve weather and climate predictions. He was the winner of the Department of Commerce Gold Medal Award in 2005 for his achievement in satellite data assimilation, and he also received the NOAA bronze medal for leading the successful NOAA-18 instrument calibration.